

## Article

# Research on Wind Load Characteristics on the Surface of a Towering Precast Television Tower with a Grid Structure Based on Large Eddy Simulation

Peng Wu <sup>1</sup>, Gang Chen <sup>2</sup>, Ruoqiang Feng <sup>1,\*</sup> and Fujiangshan He <sup>1</sup>

<sup>1</sup> Key Laboratory of Concrete and Prestressed Concrete Structures of Ministry of Education, Southeast University, Nanjing 211189, China

<sup>2</sup> The Third Construction Co., Ltd., China Construction Eighth Engineering Division, Nanjing 210023, China

\* Correspondence: hitfeng@163.com

**Abstract:** Local wind pressures on tiny rods of complex grid structures are difficult to obtain through wind tunnel tests due to their small sizes after scaling down, resulting in a lack of data support in wind load calculations for similar structures. However, local wind pressures on tiny rods can be obtained through numerical wind tunnel simulation using full-sized models. In order to investigate the wind pressure distribution of a grid structure and the influence of grid structures on the wind load of core tubes, three different television tower models are established based on an engineering example for large eddy simulations. A turbulence inlet generator (NSRFG) is adopted in the simulations while reproducing a portion of the wind tunnel test section including the mean and fluctuating pressures for validation. The results indicate that the mean wind pressures on the intersection of rods in the windward zone of the grid structure are higher than those on adjacent rods. Distinct reductions in the mean and fluctuating wind pressure of the grid structure are found in different zones. Moreover, resultant wind load forces and bending moments in the X and Y direction of the grid structure generally exceed 70% of the total wind loads. Based on simulation results, extreme net wind pressures of the grid structure and shape coefficients of enclosed regular octagonal cross-section buildings with the grid structure are provided for reference.

**Keywords:** grid structure; precast television tower; large eddy simulation (LES); numerical wind tunnel; wind load; wind pressure



**Citation:** Wu, P.; Chen, G.; Feng, R.; He, F. Research on Wind Load Characteristics on the Surface of a Towering Precast Television Tower with a Grid Structure Based on Large Eddy Simulation. *Buildings* **2022**, *12*, 1428. <https://doi.org/10.3390/buildings12091428>

Academic Editor: Theodore Stathopoulos

Received: 17 August 2022

Accepted: 7 September 2022

Published: 11 September 2022

**Publisher's Note:** MDPI stays neutral with regard to jurisdictional claims in published maps and institutional affiliations.



**Copyright:** © 2022 by the authors. Licensee MDPI, Basel, Switzerland. This article is an open access article distributed under the terms and conditions of the Creative Commons Attribution (CC BY) license (<https://creativecommons.org/licenses/by/4.0/>).

## 1. Introduction

As infrastructure and industrialization develop, more and more structures with novel shapes and structural patterns have been applied to buildings, such as the external grids of towering television (TV) towers, lattice transmission towers, and other structures. It has been recognized that geometric shapes perform a significant role in identifying the influence of wind loads on high-rise buildings [1–3]. Buildings with grid structures are generally characterized by complex shapes and interlocking rods with the interference of surrounding buildings, resulting in a highly complex wind field. Local wind pressures of buildings with complex grid structures are difficult to obtain through wind tunnel tests due to tiny rods after scaling down. Furthermore, only the mean shape coefficients of partially regularly shaped enclosed buildings are presented in the Chinese Load Code for the Design of Building Structures [4]. The wind pressure distribution and shape coefficients of complex-shaped buildings cannot be specified as well. Therefore, there is a lack of a basis in the design of wind loads, and a detailed analysis simulation should be carried out.

Many studies have been carried out in wind tunnel experiments to understand the wind load characteristics of high-rise buildings with openings and have demonstrated the importance of openings on buildings. To et al. [5] investigated the influence of two configurations of a through-building gap on the wind-induced dynamic responses of the

building. According to the results, fluctuating across-wind forces can be reduced by a disturbance of the coherence and phase-alignment of vortex excitation through the building gap. Kikitsu and Okada [6] conducted wind tunnel tests and concluded that across-wind responses of the high-rise building can be reduced by openings located in 0.8–0.9 H of the building. Li et al. [7] investigated the effect of different opening heights, opening rates, opening methods, landform types, and other influencing parameters on the wind loads of high-rise buildings. The results indicate that openings can cause the wind loads along-wind of high-rise buildings to be significantly reduced. Various aspects of the wind vibration response [8,9], drag coefficients [10,11], and shading distance [12] of lattice towers have been studied by high-frequency force-measured balance tests and aeroelastic wind tunnel tests as well. However, only a few studies have considered the wind loading effects of incoming wind flowing through the external grid structure and then acting on the main structure. Hu et al. [13] conducted aeroelastic wind tunnel tests on double-layered curtain walls with vertical slotting on the windward side. The results show that the double-layer curtain wall with vertical slotting on the windward side can effectively reduce the crosswind wind vibration response. However, the effect on the downwind response can be negligible. Shen et al. [14] investigated wind loads on a torsion-shaped high-rise building with an outer pierced ornament structure. According to the results, the mean and fluctuating wind loads on the side wind surface of the main structure can be significantly reduced due to the influence of the ornament structure. However, the spacing between the ornament structure and the main structure is small. Moreover, the size of the rods is larger than that of the TV tower. Yang et al. [15] confirmed the effectiveness of the porous double-skin facade in suppressing the across-wind responses of buildings, especially when the porous double-skin facade was located in the upper part of the building and covered at least 1/6 of the total height.

As the use of Computational Fluid Dynamics (CFD) numerical simulation grows, it becomes possible to obtain the mean and fluctuating local wind pressures on tiny rods and the wind load of the complex grid structure through large eddy simulations (LES). With recent increases in computational power and the investigation of the unsteady problem, LES has become a widely used tool for the simulation of the Atmospheric Boundary Layer (ABL) [16]. Currently, there are three main categories of LES inlet turbulence generation methods in computational wind engineering [17,18], including precursor simulation methods, recycling-rescaling-based methods, and synthetic turbulence methods. The first two methods are classified as passive inlet turbulence generation methods. Different target wind fields correspond to different wind field arrangements, which have low universality and require much time for trial-and-error simulation to control the target turbulence intensity, power spectrum, and other flow parameters. However, the turbulence synthesis method is an active simulation method. The inlet turbulence continuity conditions can be strictly guaranteed by using the random field generation (RFG) method. Furthermore, the computational accuracy and efficiency of the RFG method are relatively high. The method was first proposed by Kraichnan [19] in 1970, while later, in 2001, Smirnov et al. [20] proposed an RFG method satisfying the Gaussian spectrum by scaling an orthogonal transformation of the continuous flow field generated by the superposition of harmonic functions. Nevertheless, structural wind resistance cannot be studied using this method because it does not correspond to the ABL turbulence characteristics. Since 2010, the RFG-based methods have been developed continuously, such as Discretizing and Synthesizing Random Flow Generation (DSRFG) [21], Improved Discretizing and Synthesizing Random Flow Generation [22], Consistent Discrete Random Flow Generation (CDRFG) [23], Narrowband Synthesis Random Flow Generation (NSRFG) [24], and other methods. The expressions of the DSRFG method and CDRFG method for instantaneous wind speed are more complicated than the NSRFG method. The wavenumber parameter solution requires solving ternary quadratic equations, which takes more computational resources and a long computational time, making it challenging to apply in practical engineering. Nevertheless, the NSRFG method has a

more concise expression, and its calculation accuracy and efficiency are greatly improved, making it a more promising inlet turbulence simulation method.

Turbulent processes can be directly solved by spatially filtering the flow field on a grid scale to decompose it into two parts: large- and small-scale vortices. Large-scale vortices contain almost all the turbulent kinetic energy, and small-scale vortices mainly affect the dissipation of turbulent kinetic energy in turbulent wind fields. LES solves large-scale vortices, which can retain most of the information of vortices in turbulent motion and provide high-resolution spatiotemporal information of the flow field. Hence, the characteristics of instantaneous turbulence in the flow field can be obtained. Ji et al. [25] conducted LES simulation by the RWTR method to explore the wind effects on a standard high-rise building, including wind pressures and base bending moments. Vranešević, K.K. et al. [26] adopted validated LES and performance maps to evaluate the wind energy resources above the roof of a prismatic square building in terms of wind energy density and turbulence intensity. Numerous complex buildings have been analyzed using LES technology to validate the accuracy of different simulation methods as well [27–31].

By browsing the literature, it can be noted that few research works are available for the wind pressure distribution on specific rods of the grid structure because it cannot be obtained by aeroelastic wind tunnel tests and high-frequency force-measured balance tests, which can only obtain the overall wind load. The wind load characteristics of the external grid structure cannot be analyzed as well, causing inconveniences for the detailed design of the rods and overall structures. Furthermore, only the mean shape coefficients of partially regularly shaped enclosed buildings are presented in the Chinese Code [4]. The wind pressure distribution and shape coefficients of such buildings with grid structures cannot be specified as well. Therefore, there is a lack of a basis in the design of wind loads, and a detailed analysis simulation should be carried out.

The objective of this study is to investigate the wind characteristics around TV towers with a grid structure and wind pressure distribution characteristics of the inner and outer surfaces of the grid structure, providing a reference for the wind load values of other similar buildings. The used strategy is based on the LES using the NSRFG [24] method to generate a fluctuating velocity satisfying the turbulence characteristics of the ABL. First, the simulated flow around the building model was compared with the experimental results obtained by Dagnev and Bitsuamlak [32] to validate the accuracy and applicability of the simulation method. Later, LES numerical simulations of three TV tower models with the enclosed structure, with the grid structure, and without the grid structure at different wind direction angles are conducted. Wind pressure characteristics on the inner and outer surfaces of the grid structure are investigated. The influence of the grid structure on the wind pressure distribution and the wind load force of the core tube structure is analyzed as well. In the end, based on simulation results, extreme net wind pressures of the grid structure and shape coefficients of enclosed regular octagonal cross-section buildings with the grid structure are provided for reference.

This paper consists of five sections. Section 2 introduces three TV tower models used for simulation. Next, Section 3 introduces the numerical simulation method satisfying targeted inlet turbulence characteristics. Furthermore, the mean and fluctuating wind pressures of the building model are validated. Numerical simulation results are presented in Section 4, beginning with a general description of the velocity field around three TV towers, and then the local wind pressure characteristics of the TV tower with the grid structure are given. The paper closes with conclusions about wind pressure distribution and the influence of grid structures on the core tube in Section 5.

## 2. Project Overview

### 2.1. Model Description

TV tower models are established based on a steel towering precast TV tower without the building envelope in China with a total height of 220.0 m, consisting of a communication tower and a mast, as shown in Figure 1. The communication tower is located within the

elevation range from 0 m to 161.7 m, and the mast is located within the elevation range from 161.7 m to 220.0 m. The communication tower consists of an internal core tube and an external grid structure. The core tube is regular octagonal in a cross-section with a maximum radial dimension of 6.6 m. The horizontal cross-sectional outline of the external grid structure is hexagonal, and its rods are made of thin-walled rectangular steel pipes. The overall shading factor of the grid structure is approximately 0.8. The maximum horizontal width is 33.5 m, located at the bottom of the TV tower at 0 m, and the minimum width is 9.5 m, located at 83.6 m. The spherical upper man tower is located within an elevation range of 136.6 m to 161.7 m, with a maximum diameter of 26 m. The horizontal cross-section profile of the mast is octagonal at the bottom and quadrilateral at the top, and the width changes from 5.5 m to 1.2 m as the height increases. Three models with an enclosed structure, with a grid structure, and without a grid structure, respectively, are established to investigate the wind pressure characteristics of the TV tower, as shown in Figure 2.

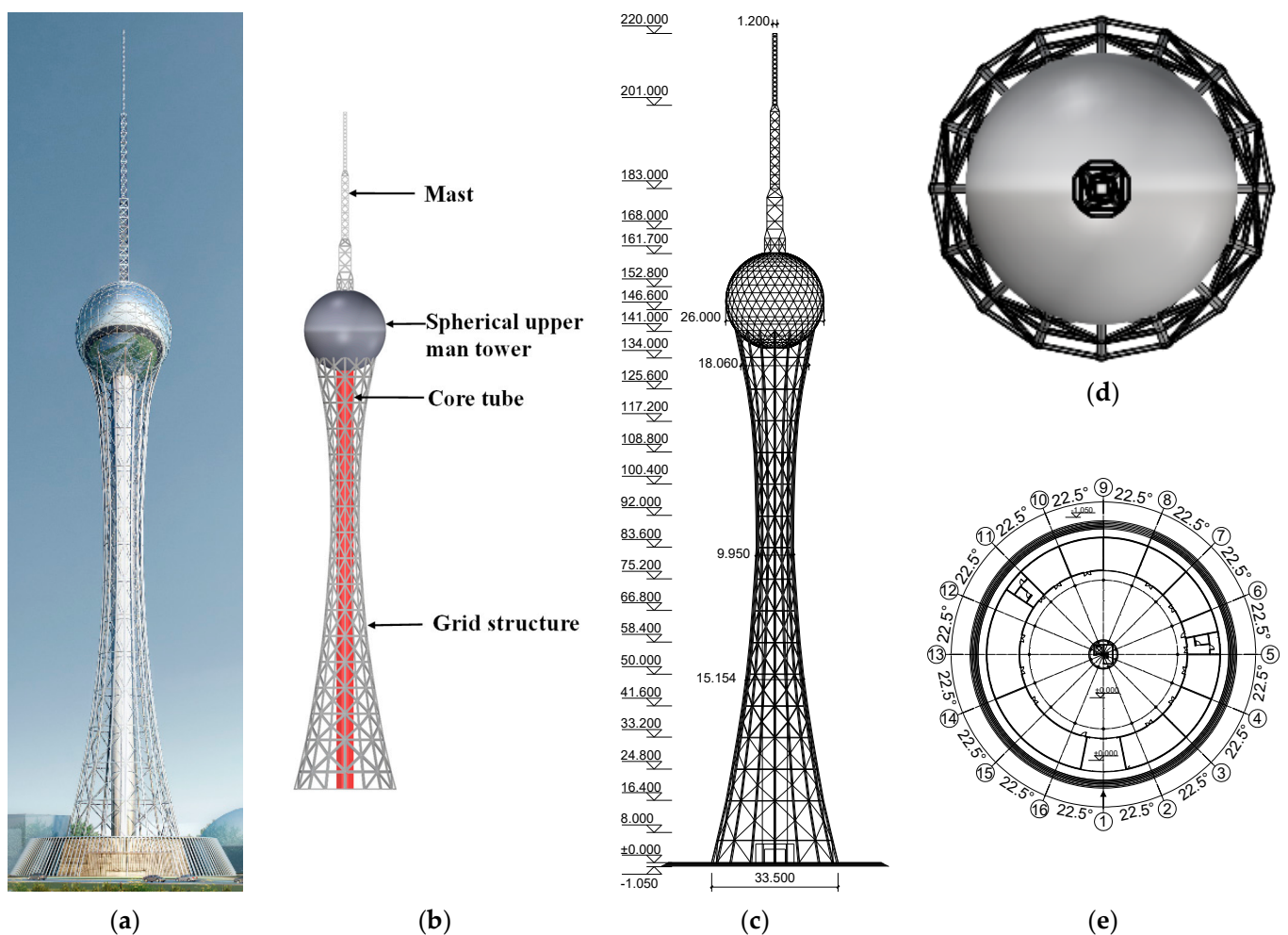


**Figure 1.** Architectural rendering, 3D model drawing, elevation drawing, top view, and ground floor plan of the TV tower: (a) Architectural rendering; (b) 3D model drawing; (c) Elevation drawing; (d) Top view; (e) Ground floor plan.

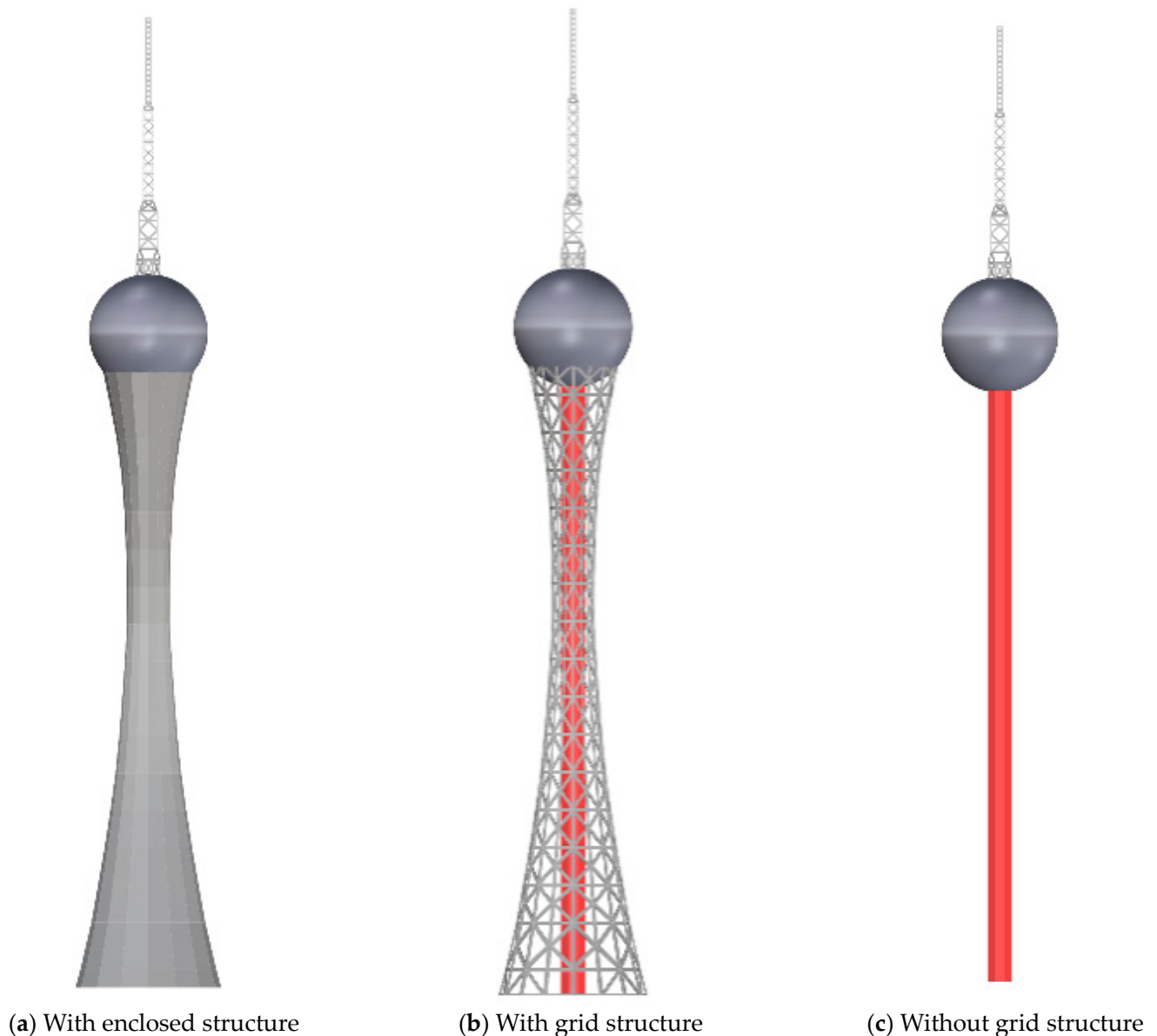


**Figure 2.** Three types of TV tower models.

## 2.2. Measuring Points Arrangement

Six layers of measuring points were arranged at 25 m, 50 m, 75 m, 83.6 m, 100 m, and 125 m, respectively. A total of 8 measuring points were arranged on each layer of the core tube, and 64 measuring points were arranged on the inner and outer surfaces of the grid structure at the corresponding height, with 432 measuring points. The TV tower cross-section is center-symmetric, and the structure is center-symmetric as well. In terms of the complexity of the structure, the wind direction angles were determined to be  $0\sim 90^\circ$ , with an interval of  $15^\circ$ . Figure 3 illustrates the arrangement of measuring points on the 25 m layer and the definition of wind direction angles. The rest of the five layers were arranged in the same way. The maximum radial size of each layer is presented in Figure 4. The mean and fluctuating wind pressure coefficients of measuring point  $i$  are expressed by  $\bar{C}_{pi}$  and  $C_{\sigma pi}$ , respectively, and calculated according to Equation (1). Positive values indicate pressure, and negative values indicate suction. Since the inner and outer surfaces of the grid structure are subject to wind loads, it is necessary to consider the net wind pressure ( $C_{npi}$ ) calculated according to Equation (2), where  $C_{opi}$  is the wind pressure

coefficient on the outer surface and  $C_{ipi}$  is the corresponding wind pressure coefficient on the inner surface.

$$C_{pi} = \frac{P_i}{0.5\rho U_H^2}, \bar{C}_{pi} = \frac{\bar{P}_i}{0.5\rho U_H^2}, C_{\sigma pi} = \frac{\sigma_p}{0.5\rho U_H^2} \quad (1)$$

$$C_{npi} = C_{opi} - C_{ipi} \quad (2)$$

where  $P_i$  is the instantaneous static wind pressure at the  $i$  monitoring point on the surface of the building;  $\rho$  is the air density;  $U_H$  is the mean wind velocity at the reference height (take the top of the TV tower height of 220 m corresponding to the velocity of 40.22 m/s);  $\bar{P}_i$  is the mean static wind pressure over the time history of the  $i$  measuring point;  $\sigma_p$  is the root mean square of the pressure-time history of the measuring point.

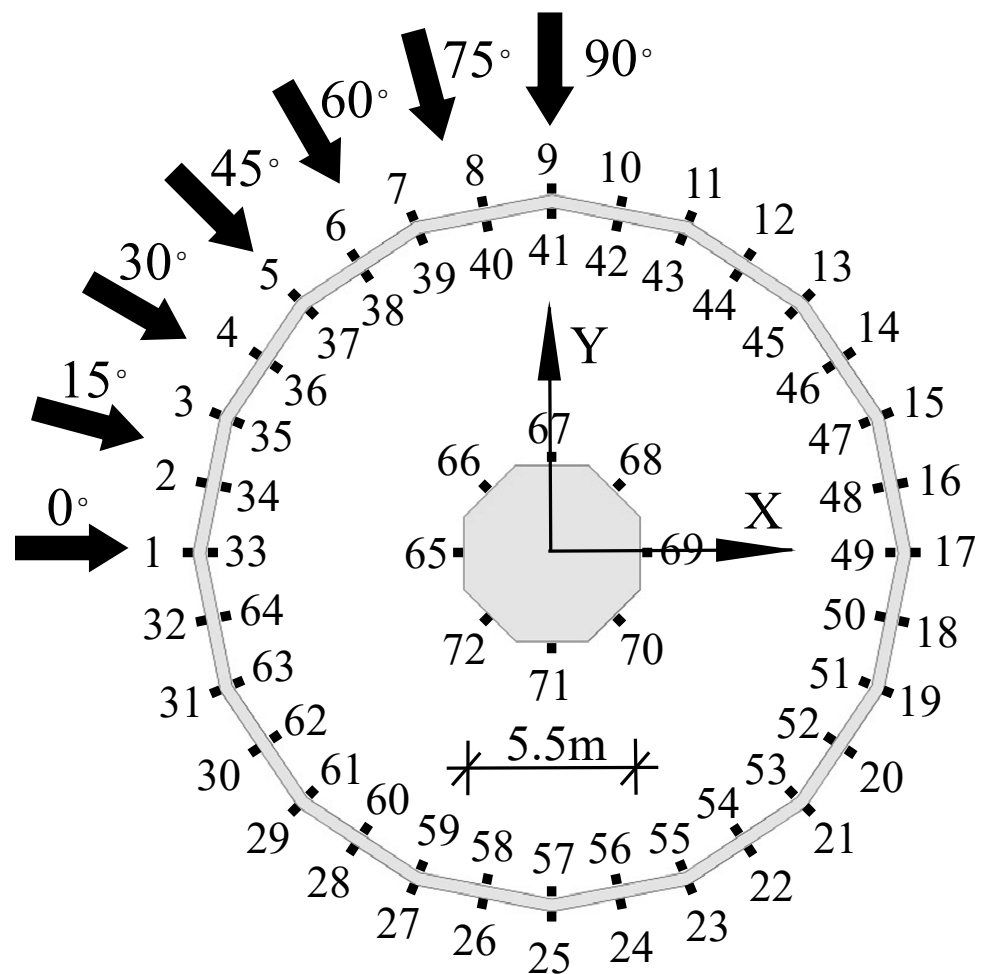


**Figure 3.** Arrangement of the measuring points on the 25 m layer and the definition of wind direction angles.

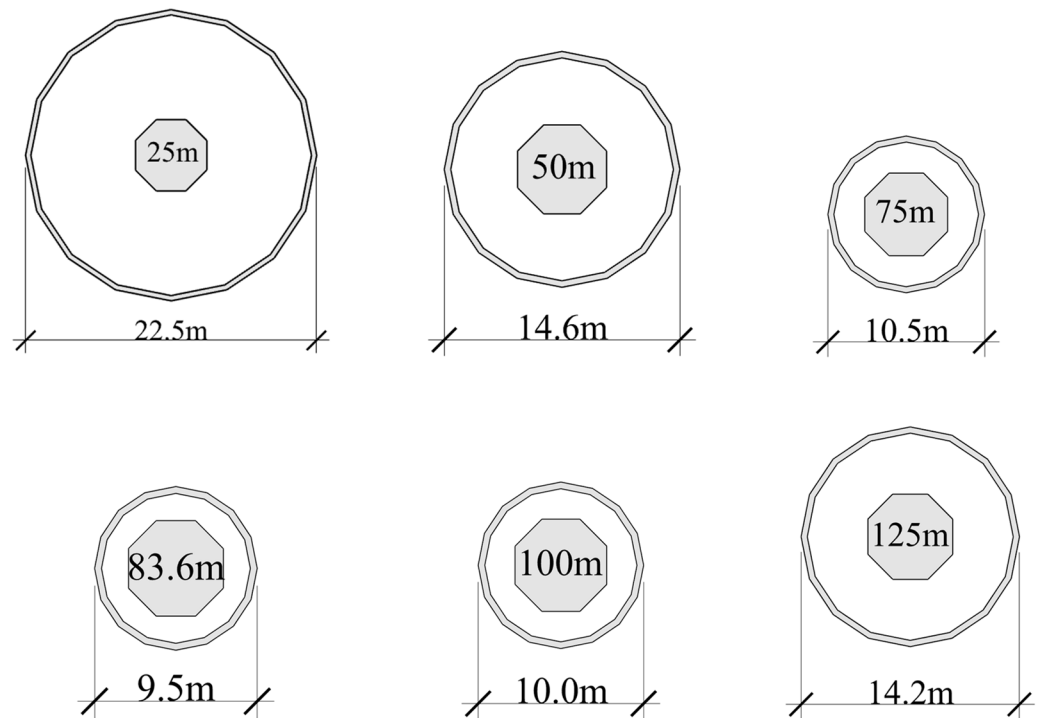


Figure 4. Cross-sectional dimension of each measuring point layer.

### 3. Numerical Simulation

#### 3.1. Introduction of NSRFG

The fluctuating wind velocity time history of a single point can be viewed as a smooth random process superimposed by several harmonic units of different frequencies by the principle of harmonic superposition. The basic idea of the NSRFG method is to correspond each harmonic unit to a narrow-band process. Then, sufficient harmonic units with simulation accuracy are selected to reconstruct the fluctuating wind velocity time history, satisfying the requirements by the method of time-domain superposition. Finally, the fluctuating velocity is extended to a three-dimensional space, meeting the turbulent characteristics of ABL by considering the spatial correlation in a simulation of a single-position fluctuating velocity-time history. The expression of instantaneous wind velocity in the NSRFG method is shown in Equation (3):

$$u_i(x, t) = \sum_{n=1}^N P_{i,n} \sin \left( k_{j,n} \frac{x_j}{L_{j,n}} + 2\pi f_n t + \phi_n \right) \tag{3}$$

where  $u_i$  ( $i = 1, 2,$  and  $3,$  respectively) represents the velocities in the along-wind, across-wind, and vertical directions, respectively;  $x = \{x, y, z\}$  is the coordinate vector;  $t$  is time;  $N$  is the number of spectral segments;  $f_n = \frac{(2n-1)}{2} \Delta f$ ;  $\Delta f$  is the frequency bandwidth;  $\phi_n \sim U(0, 2\pi)$  is a random number with a uniform distribution between  $0$  and  $2\pi$ ;  $L_{j,n} = \frac{U_{av}}{f_n c_j \gamma_j}$ , where  $c_j$  is the decay coefficient of the target spatial correlation in the  $j$  direction ( $j = 1, 2,$  and  $3$  denote the  $x, y,$  and  $z$  directions, respectively);  $\gamma_j$  is the tuning factor used to adjust the spatial correlation of the generated turbulence flow field to satisfy the target condition.  $k_n = \{k_{1,n}, k_{2,n}, k_{3,n}\}$  is a vector with a uniform distribution on a spatial circular curve, which can be calculated by Equation (4).

$$\begin{cases} k_{1,n} = -\frac{q_{2,n}^2 + q_{3,n}^2}{A_n} \sin \theta \\ k_{2,n} = \frac{q_{1,n} q_{2,n}}{A_n} \sin \theta + \frac{q_{3,n}}{B_n} \cos \theta \\ k_{3,n} = \frac{q_{1,n} q_{3,n}}{A_n} \sin \theta - \frac{q_{2,n}}{B_n} \cos \theta \end{cases} \tag{4}$$

where  $q_{i,n} = \frac{P_{i,n}}{L_{i,n}}$  ( $i = 1, 2, 3$ );  $A_n = \sqrt{(q_{2,n}^2 + q_{3,n}^2)^2 + q_{1,n}^2 q_{2,n}^2 + q_{1,n}^2 q_{3,n}^2}$ ;  $B_n = \sqrt{q_{2,n}^2 + q_{3,n}^2}$ ;  $P_{i,n} = \sqrt{2S_{u,i}(f_n)\Delta f}$ ;  $S_{u,i}(f_n)$  is the Von Karman spectrum in the  $i$  direction at the frequency  $f_n$ , which can be calculated by Equation (5). The Von Karman spectrum can be adapted to reflect the statistical properties of the fluctuating wind speed. The expressions of the fluctuating wind speed spectra in three directions of  $u$ ,  $v$ , and  $w$  are as follows:

$$S_u(f) = \frac{4(I_u U_{av})^2 (L_u / U_{av})}{[1 + 70.8(fL_u / U_{av})^2]^{5/6}} \quad (5a)$$

$$S_v(f) = \frac{4(I_v U_{av})^2 (L_v / U_{av}) [1 + 188.4(2fL_v / U_{av})^2]}{[1 + 70.8(2fL_v / U_{av})^2]^{11/6}} \quad (5b)$$

$$S_w(f) = \frac{4(I_w U_{av})^2 (L_w / U_{av}) [1 + 188.4(2fL_w / U_{av})^2]}{[1 + 70.8(2fL_w / U_{av})^2]^{11/6}} \quad (5c)$$

where  $U_{av}$  is the mean wind velocity, and  $I$  and  $L$  are the turbulence intensity and turbulence integral scale in three directions, respectively.

The flowchart of the NSRFG method is shown as follows Figure 5:

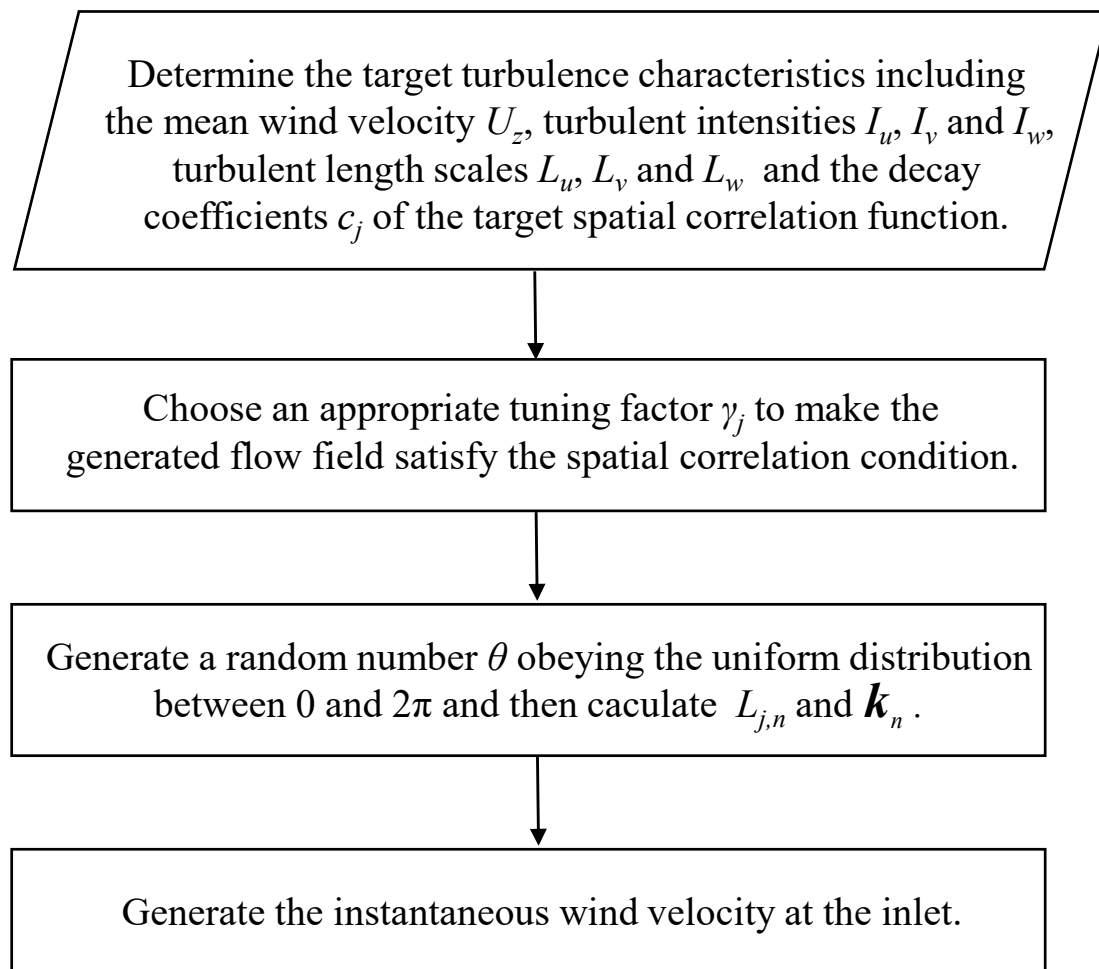


Figure 5. Flowchart of the NSRFG method.

### 3.2. Validation of the NSRFG Method on the CAARC Standard Model

#### 3.2.1. Computational Domain and Boundary Conditions

The NSRFG method was adopted to generate the fluctuating wind field in the ABL and then applied to the simulation of the Commonwealth Advisory Aeronautical Research Council (CAARC) standard building. The simulation results were compared with the experimental results of Dagneu and Bitsuamlak [32] to validate the accuracy and applicability of the NSRFG method on LES simulations. The size of the CAARC model is  $0.076(D_x) \times 0.1143(D_y) \times 0.4572$  m (H), with a scale factor of 1:400. The dimension of the computational domain is  $3.8481 \times 1.9431 \times 1.1430$  m, and the blockage ratio on the windward side is 2.35% less than 5% [33]. The dimensions and boundary conditions of the computational domain are shown in Table 1 and Figure 6.

**Table 1.** Boundary conditions.

Boundary	Definition
Inlet	Velocity-inlet
Outlet	Outflow
The top surface of the computational domain	Symmetry
The side surface of the computational domain	Symmetry
The bottom surface of the computational domain	No-slip wall
The surface of CAARC	No-slip wall

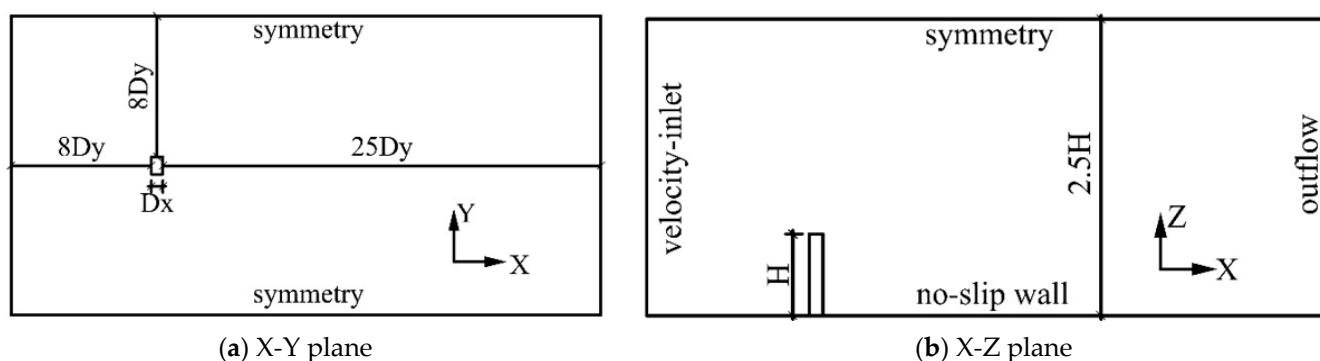


**Figure 6.** Dimensions and boundary conditions of the computational domain.

#### 3.2.2. Solution Method and Meshing

The computational domain was divided into several parts to obtain a high-quality mesh by using structural grids for the whole computational domain. Two  $D_y$  lengths were extended from the CAARC model into the space, forming the core grid encryption region, as shown in Figure 7. Two grid schemes, G1 and G2, were adopted to study the grid independency of the results. The stretching ratio of the grids in the core grid encryption regions of the G1 and G2 schemes is 1.15 and 1.05, respectively. The stretching ratio of the grids outside the encryption region is increased to 1.2 to reduce the computation time. In terms of the simulation of the empty domain, approximately 1.4 million structural grid cells were generated for grid G1, and 2.1 million were generated for grid G2, as shown in Figure 8 (only grid scheme G1 is presented in Figure 7). The height of the first grid layer on the surface of the building was determined to be  $1 \times 10^{-4}$  m in consideration of the computational resources. The  $y^+$  value near the wall surface was approximately 3.6 less than 5, and the cut-off error of the wave number was minimized in the LES modeling [34], which was acceptable for the wall function. The quality of the computational grids of two grid schemes is in the range of 0.7 to 1.0.

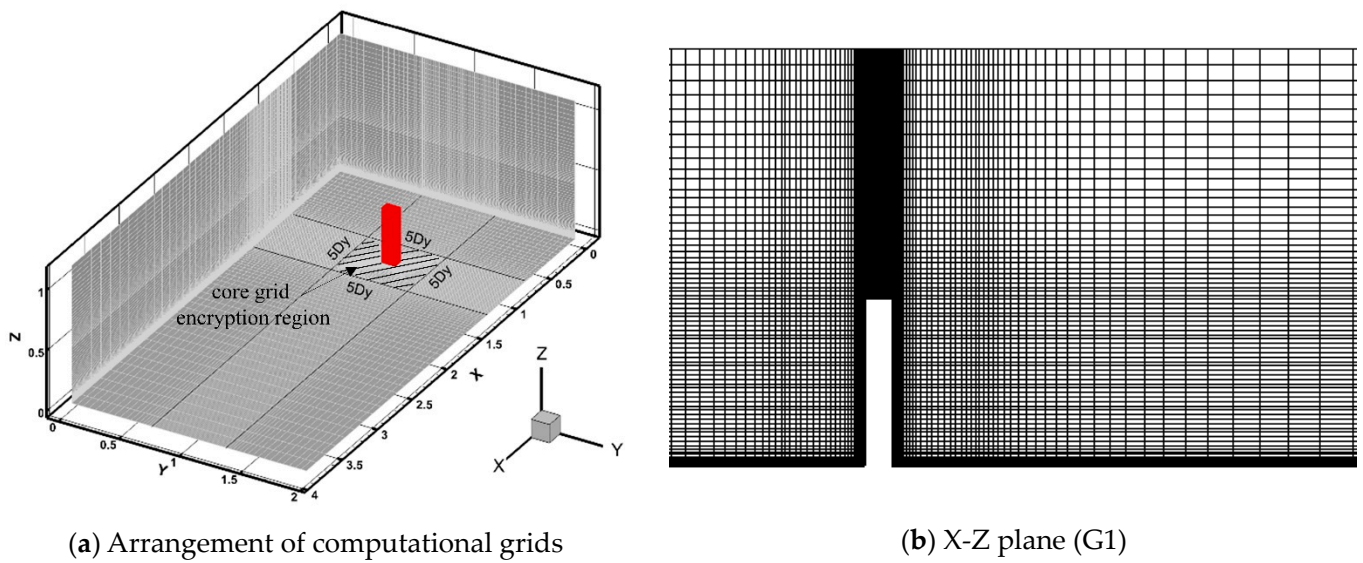


Figure 7. Computational grid for the CAARC building model.

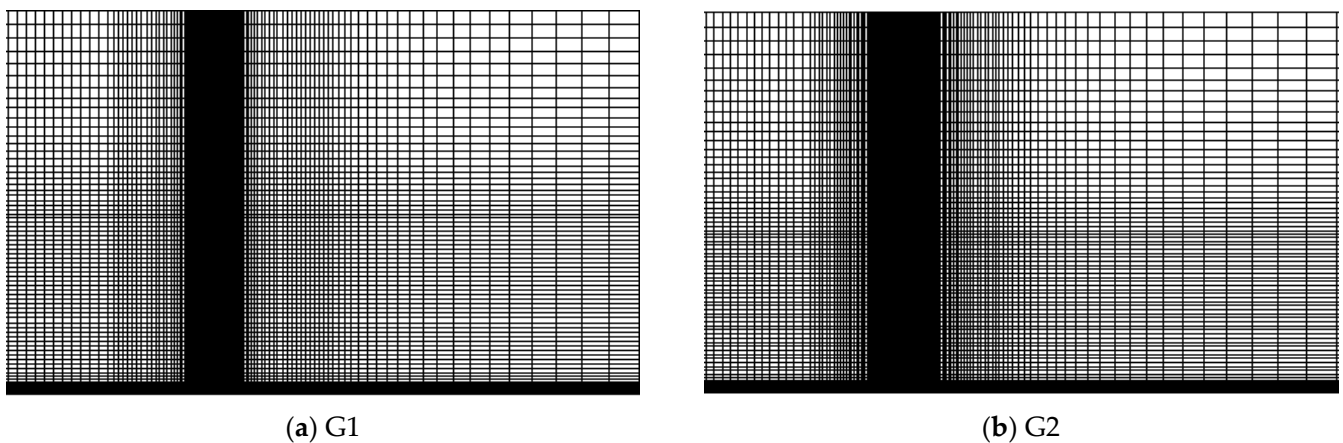


Figure 8. Computational grids for the empty domain.

The discrete system of the continuity equation derived from the law of conservation of mass is solved using the SIMPLEC algorithm based on the semi-implicit method for solving the pressure-coupled systems of equations, which has good convergence and is suitable for LES calculations with small time steps [35]. The time derivative was discretized by the second-order implicit scheme, and the momentum discretization was discretized by the bounded central difference scheme. The wall-adapting local eddy-viscosity model was selected as the subgrid-scale model for LES. An absolute velocity residual of less than  $10^{-5}$  was adopted to ensure the convergence of the simulation. The time step for the transient LES calculation was selected as  $1 \times 10^{-4}$  s considering the mesh discretization and computational resources. The maximum and average Courant numbers near the ground are 0.865 and 0.124, respectively, ensuring the time accuracy of the simulation. A total of 40,000 time steps were set to provide a statistically steady result of 4 s. The simulated results were sampled after an initialization period of 0.5 s.

### 3.2.3. Target Turbulence Characteristics

Since the NSRFG method is based on the Von Karman spectrum to generate turbulent inlet velocities, the mean wind profile, turbulence intensity, and turbulence integral scale in the along-wind, across-wind, and vertical directions of the target wind characteristics of the turbulent wind field should be determined before simulation. The turbulence characteristics of the ABL for the wind tunnel test were measured, as shown in Table 2.

**Table 2.** Measured inflow wind characteristics of the rural terrain.

Height (m)	Mean Velocity (m/s)	Turbulent Intensity (%)	Turbulence Integral Scale (m)
		$I_u$	$L_u^x$
0.1524	10.381	24.00	0.480
0.3048	11.458	22.50	0.540
0.4572	12.061	21.00	0.550
0.6096	12.810	19.60	0.600
0.9144	13.647	16.90	0.630
1.2192	14.438	15.60	0.640

The specific turbulence characteristic parameters at the inlet are presented in Table 3. The mean wind profile was recommended in the form of an exponential law with an exponent of 0.16 [32]. The reference height was taken as the top of the building (0.4572 m), and the corresponding wind velocity was 12.061 m/s. The turbulence intensity and along-wind turbulence integral scale were in the form of an exponential law as well. The recommended values of Engineering Sciences Data Unit (ESDU) 85,020 [36] were adopted for the turbulence intensity and turbulence integral scales of the fluctuating components  $v$  and  $w$ . Comparisons of the mean wind speed profile, along-wind turbulence intensity, and along-wind turbulence integral scale using the exponential form with the experimental values presented in Table 2 are shown in Figure 9, indicating that the fitted values are representative of the experimental values. The integral scale was corrected near the wall surface to increase the point where the near-wall area sub-scale was equal to zero and was more consistent with the actual fluctuating wind field. The spatially relevant parameters of the NSRFG method took the following values:  $c_1 = 10$ ,  $c_2 = 10$ ,  $c_3 = 15$ ,  $c_3 = 15$ ,  $\gamma_1 = 3.2$ ,  $\gamma_2 = 1.6$ ,  $\gamma_3 = 1.4$ . The number of spectral segments  $N$  was chosen as 2000.

**Table 3.** CAARC model numerical simulation of turbulent wind field parameter settings.

Parameters	Definitions
Mean velocity	$U_{av}(z) = U_{ref} \left( z/z_{ref} \right)^\alpha$ , $U_{ref} = 12.061$ m/s, $z_{ref} = 0.4572$ m, $\alpha = 0.16$
Turbulence intensity	$I_u(z) = I_{ref} (z/0.3048)^{-\beta}$ , $I_{ref} = 0.225$ , $\beta = 0.26$ $I_v(z) = I_u(z) \frac{\sigma_v}{\sigma_u}$ , $I_w(z) = I_u(z) \frac{\sigma_w}{\sigma_u}$ $L_u(z) = 0.54 \left( \frac{z}{0.3048} \right)^{0.14}$ ,
Turbulence integral scales	$L_v(z) = 0.5 \left( \frac{\sigma_v}{\sigma_u} \right)^3 L_u(z)$ , $L_w(z) = 0.5 \left( \frac{\sigma_w}{\sigma_u} \right)^3 L_u(z)$

where  $\frac{\sigma_v}{\sigma_u} = 1 - 0.22 \cos^4 \left( \frac{\pi z}{2h} \right)$ ,  $\frac{\sigma_w}{\sigma_u} = 1 - 0.45 \cos^4 \left( \frac{\pi z}{2h} \right)$ ,  $h = \frac{u_*}{0.7}$ ,  $u_* = V_{10} / [2.5 \ln(10/z_0)]$ ,  $f = 2 \times 72.9 \times 10^{-6} \sin \varphi$ ,  $\varphi$  (Latitude of the region).

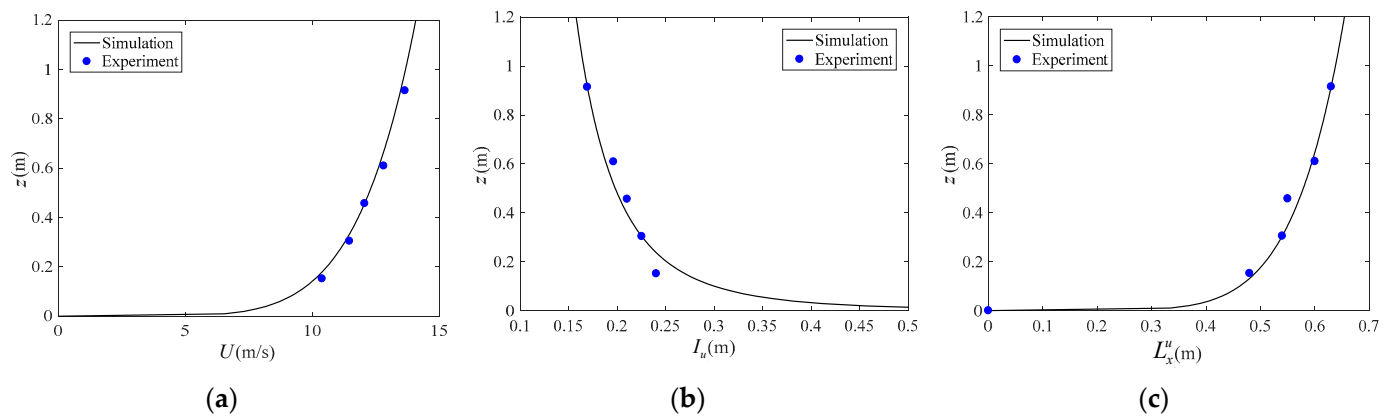


**Figure 9.** Comparison of turbulence characteristics at the inlet boundary using the exponential form with the experimental values: (a) Mean wind speed profile; (b) Along-wind turbulence intensity profile; (c) Along-wind turbulence integral scale.

### 3.2.4. Simulation Results

Twenty points were arranged vertically from low to high at the center point coordinates (0.9542 m, 0.97155 m, 0 m) of the CAARC model placed at an interval of 0.05 m to monitor the simulated velocity characteristics. In addition, two groups of twenty points were arranged at the inlet ( $x = 0$  m) and halfway between the inlet and the center of the CAARC model ( $x = 0.4711$  m), respectively, to test the homogeneity of the mean wind velocity and turbulence intensity profiles. The locations of monitoring points are shown in Figure 10.

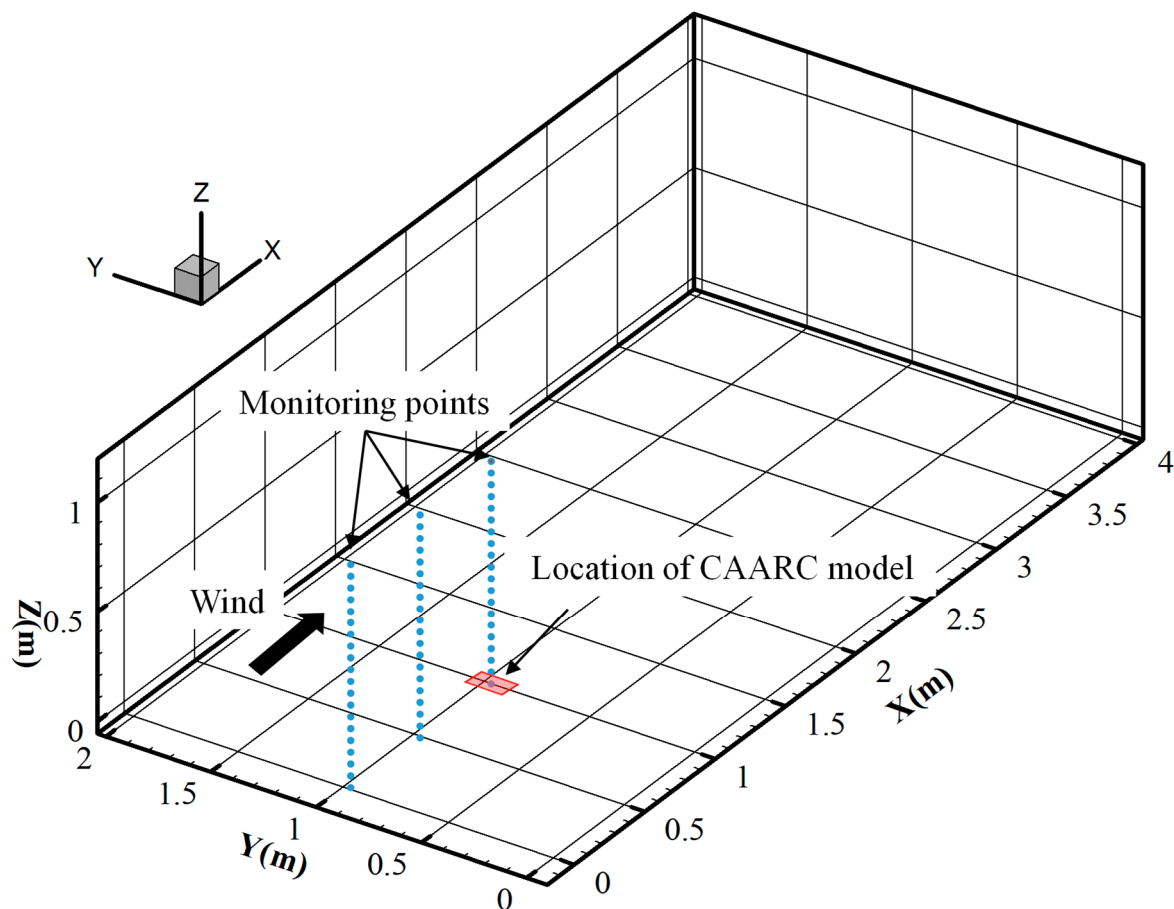


**Figure 10.** Location of monitoring points.

The mean wind velocity and turbulence intensity profiles at the center position of the CAARC model placed can be derived from the velocity-time history of each monitoring point, as shown in Figure 11. A 1.9% difference and a 3.2% difference are observed between G1 and G2 in the mean wind velocity and turbulence intensity profiles, respectively. Hence, the results of the CAARC model simulations in the following sections are all based on G1. The mean wind velocity profile in the central area of the building model is consistent with the target velocity profile specified in Section 3.2.3. However, the turbulence intensity profile is slightly attenuated. In order to investigate the homogeneity of profiles between the inlet and building position, the mean wind velocity and turbulence intensity profiles at different positions are presented in Figure 12. As the distance from the inlet increases, there is almost no decay in the mean wind velocity, but the turbulence intensity gradually attenuates. The turbulence intensity at the inlet ( $x = 0$  m) is, on average, 5.0% and 10.8% higher than that at the middle position ( $x = 0.4711$  m) and the position of the building ( $x = 0.9542$  m), respectively, which is mainly related to the wind velocity time equation not fully satisfying the momentum equation, LES filtering, subgrid-scale model, wall mathematical model, and meshing accuracy simulated by the NSRFG method. Nevertheless, the turbulence intensity profile at the position of the building placed agrees with the experimental results in general.

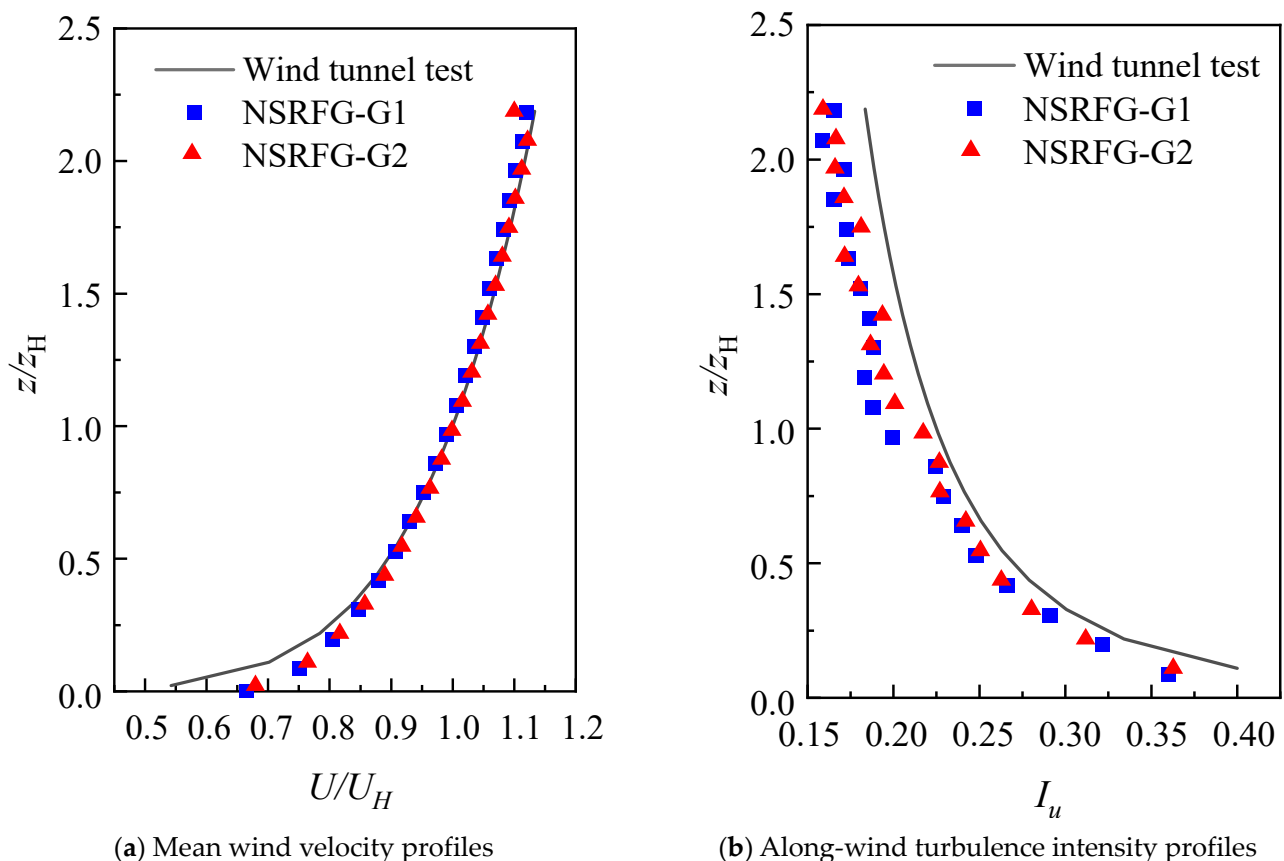


**Figure 11.** Mean wind velocity and turbulence intensity profiles at the center position of the CAARC model placed.

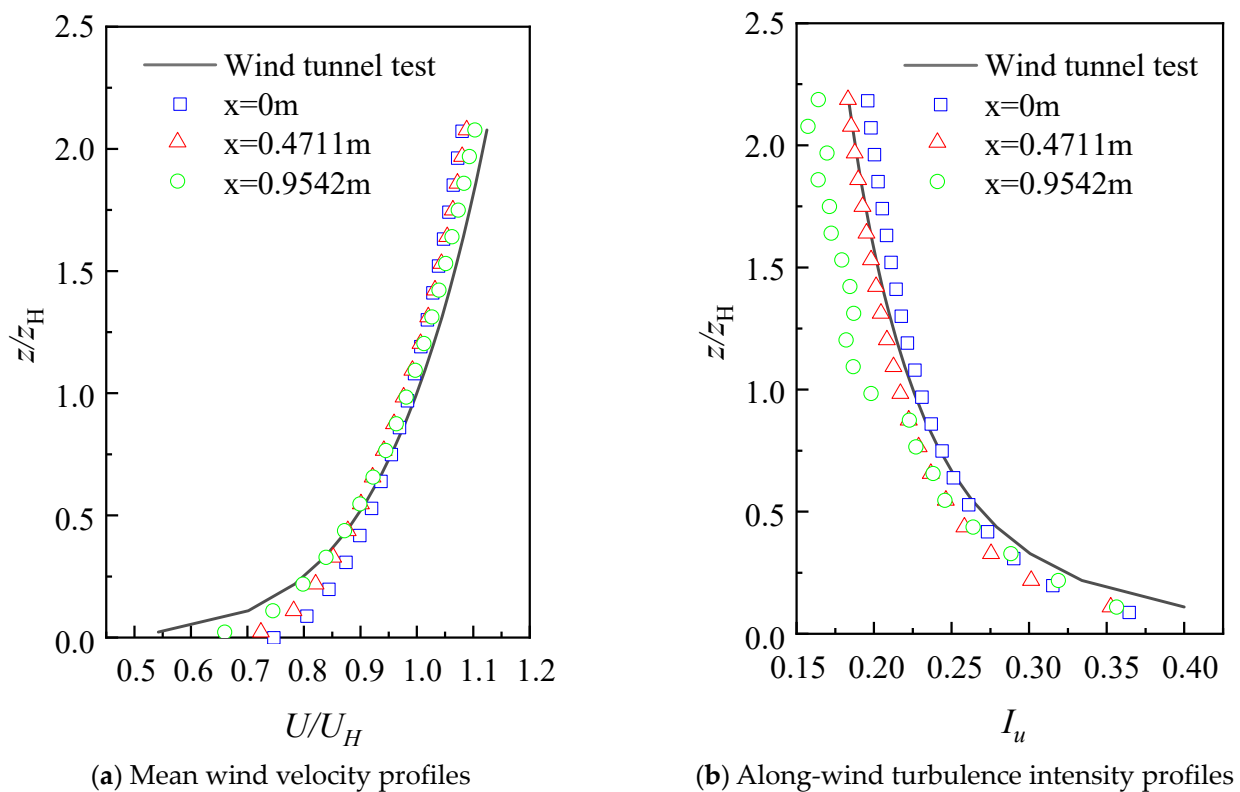


**Figure 12.** Mean wind velocity and turbulence intensity profiles at different locations.

The 0–4 s along-wind velocity time history and the normalized power spectral density of the monitoring point  $Z_1$  (0.9542 m, 0.97155 m, 0.4572 m) of G1 are shown in Figure 13. It can be observed that the monitored values of the power spectral density at the model location only agree well with the target values in the low-frequency region, while they decay rapidly in the high-frequency region. This phenomenon is related to the turbulent kinetic energy dissipation generated by the filter operation of LES on small-scale vortices. The filtering scale is determined by the grid resolution and calculation time step. Due to computational resources, relatively coarse grids, large time steps, and short iteration times are determined, causing the length scale of the monitoring point to be smaller than the filtering scale. The energy supplied by the fluctuation of this part cannot be calculated directly, resulting in the early truncation of the energy spectrum. Nevertheless, the natural vibration frequency of structures is generally between 0.1 Hz and 5 Hz. The American [37] and Australian [38] load codes specify that when the natural vibration frequency of the structure is greater than 1 Hz, the effect of wind vibration can be disregarded. Therefore, the primary concern of structural wind engineering is the fluctuating wind velocity power spectra in the frequency band of 0.1 Hz to 1 Hz. In conclusion, the simulation of the equilibrium ABL turbulent wind field agrees with the requirements in general.

The arrangement of measuring points at  $2/3 H$  of the CAARC standard model is shown in Figure 14. The mean wind pressure coefficients on the three elevations at  $2/3 H$  of the CAARC model simulated by the numerical wind tunnel are shown in Figure 15. It can be observed that the distributions of mean wind pressure coefficients obtained from the simulation and experiment on the windward side both present a trend of a large top and a small bottom, with a mean deviation rate of approximately 5.3%. On the leeward side, the mean wind pressure coefficients simulated are closer to the distribution trend obtained from the experiment, with a mean deviation rate of about 6.1%. On the lateral side, the simulated mean wind suction forces are larger than the experimental values, and the mean deviation rate is about 9.1%.

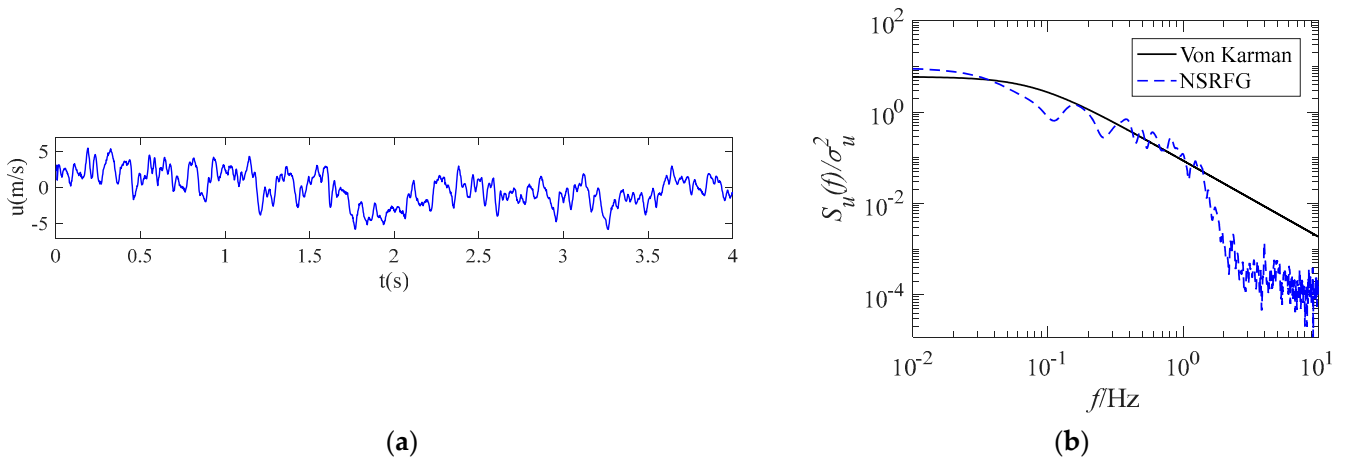


**Figure 13.** Wind velocity–time history and normalized power spectral density of the monitoring point  $Z_1$ : (a) 0–4 s along–wind fluctuating velocity–time history; (b) Spectra of the along–wind fluctuating wind velocity.

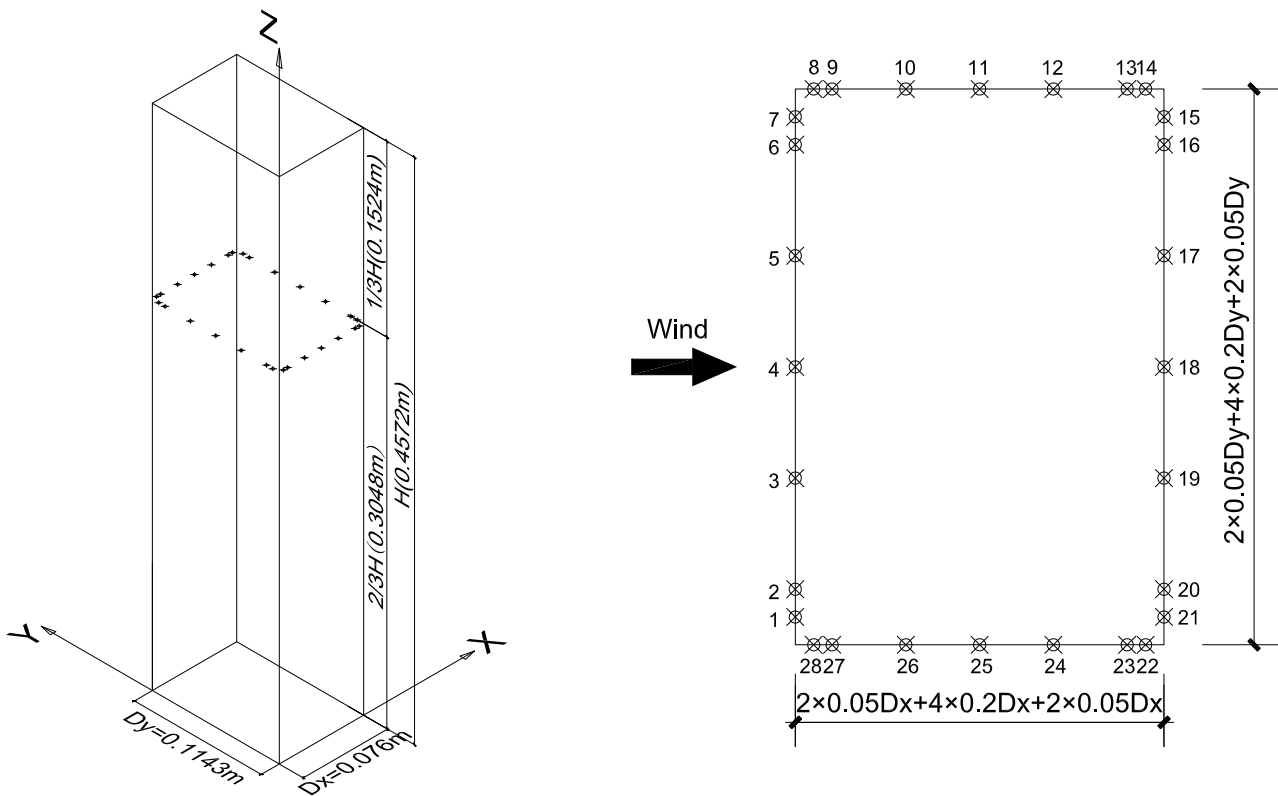


**Figure 14.** Arrangement of measuring points at  $2/3 H$  of the CAARC model.

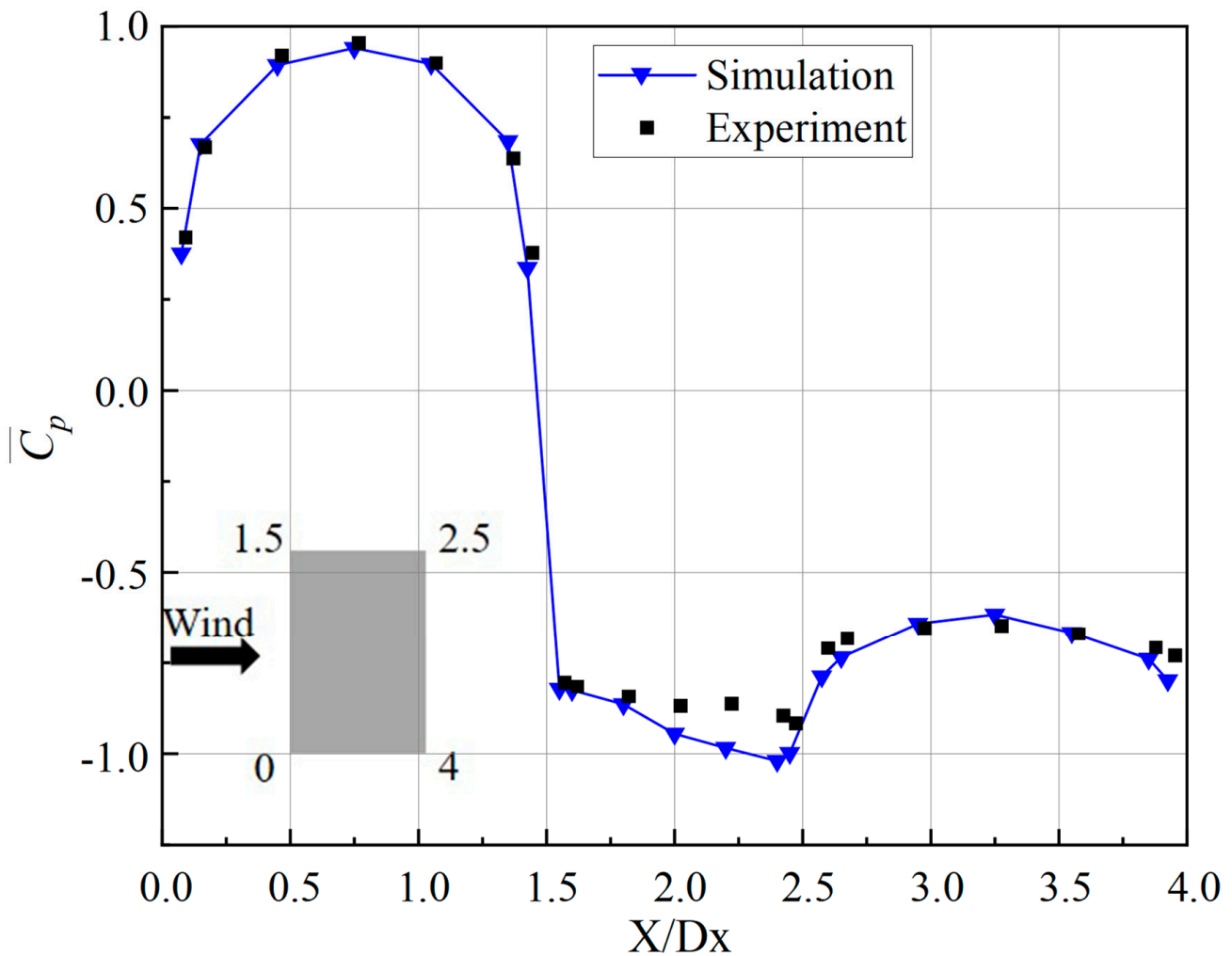


Figure 15. Comparison of mean pressure coefficients at  $2/3 H$  of the CAARC model.

The distribution of wind pressure coefficients under different working conditions is shown in Figures 16 and 17. The mean wind pressure coefficients at the same height of the windward side under each working condition are consistent with the wind tunnel test results, while the fluctuating wind pressure coefficients are larger. The distribution of the fluctuating wind pressure coefficients on the leeward side is relatively uniform. However, the fluctuating wind pressure coefficients are larger compared with the wind tunnel experiment, mainly because the flow field in the computational domain is a high Reynolds number flow field. Moreover, the fluctuating flow field is unstable, and there is an inevitable error between the target turbulence characteristics and the measured data in the wind tunnel test.

In conclusion, the NSRFG method adopted in this study can reasonably simulate the mean and fluctuating winds, satisfying the turbulence characteristics of the ABL, which validates the accuracy and applicability of the simulation method in this study.

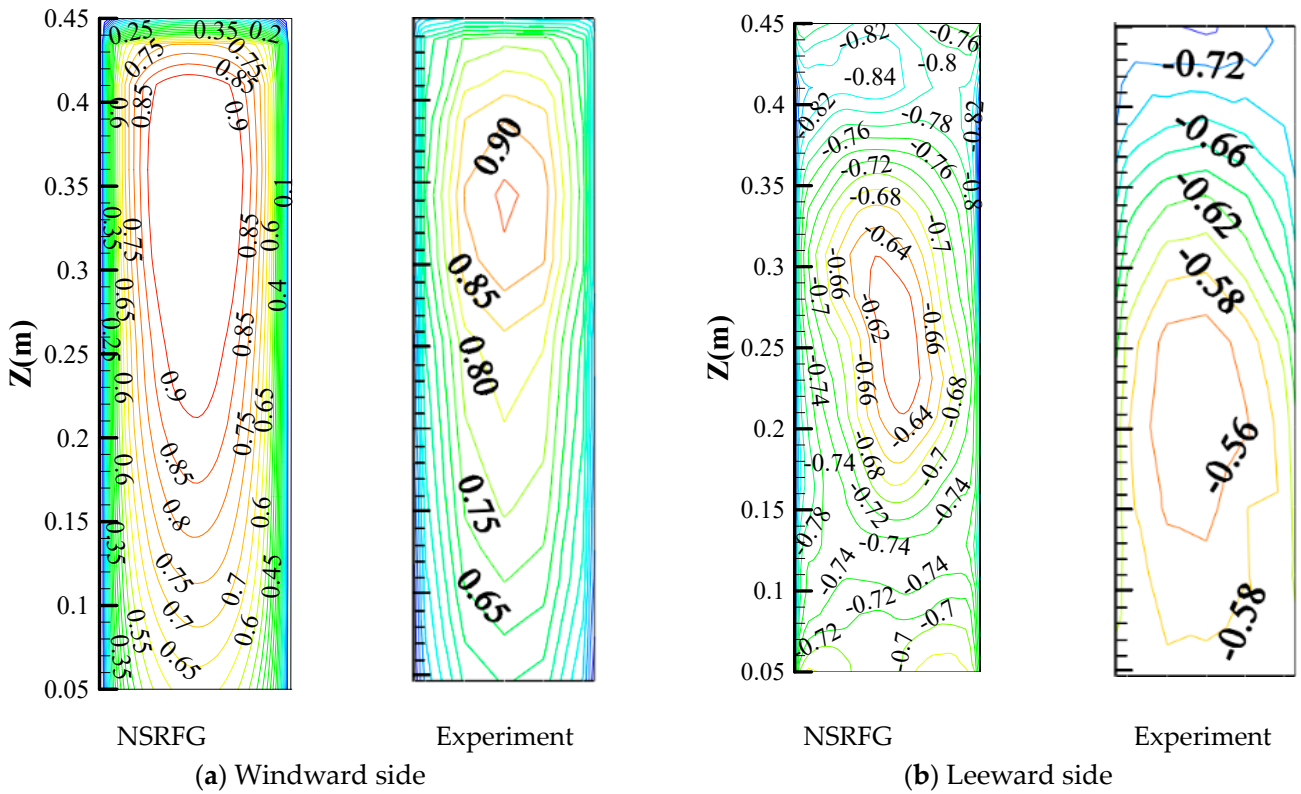


Figure 16. Contours of the mean wind pressure coefficients on the windward and leeward sides.

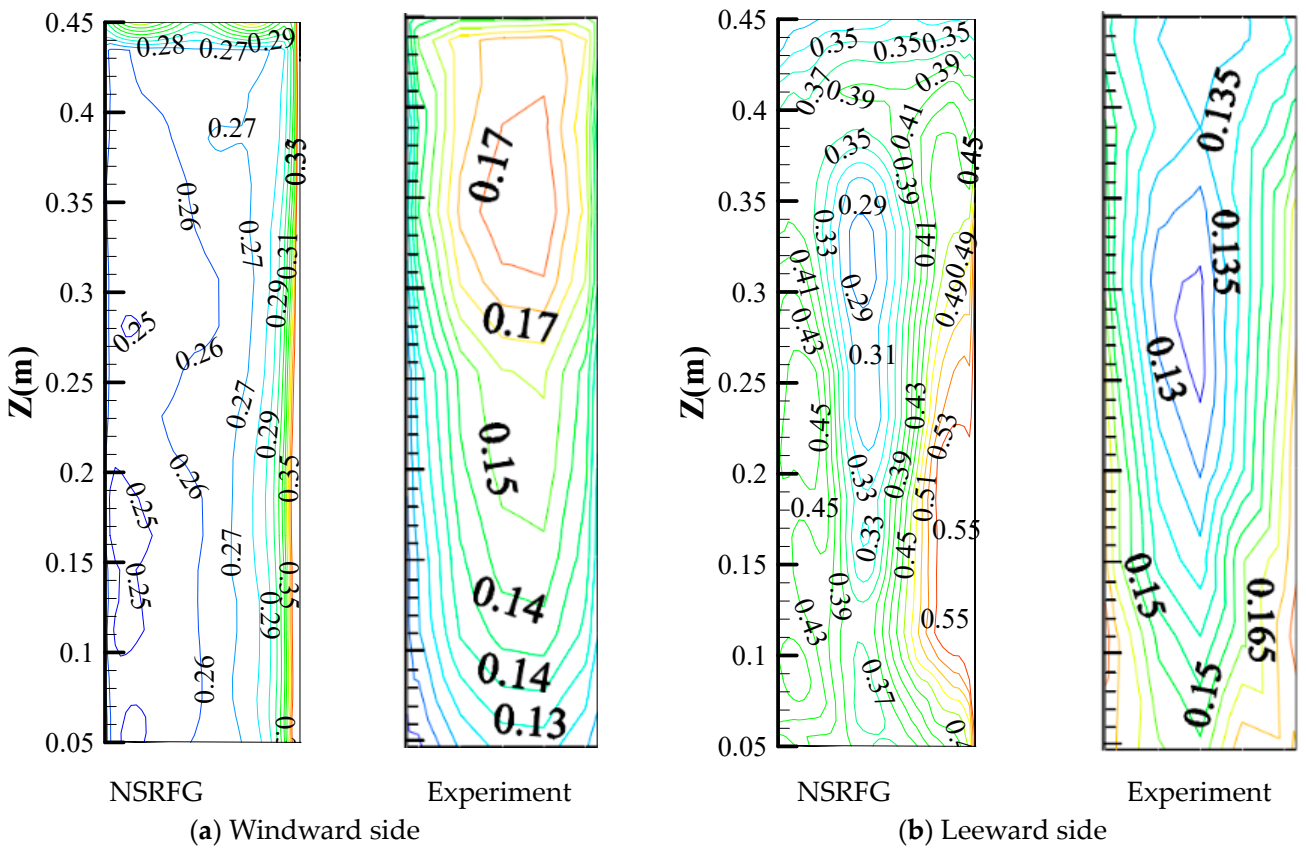


Figure 17. Contours of the fluctuating wind pressure coefficients on the windward and leeward sides.

### 3.3. LES of the Towering Precast TV Tower without a Building Envelope

The computational domain and boundary conditions of the full-scale model are presented in Figure 18. The computational domain is a cuboid with dimensions of  $800 \times 400 \times 500$  m in the  $x$ ,  $y$ , and  $z$  directions and a blockage ratio of less than 3% [33]. A mixed inner and outer domain meshing scheme was applied to divide the computational domain because of complex rods outside the core tube, as shown in Figure 19. The surface of the building model was gridded with three layers of prismatic grids, and the height of the first wall grid was selected to be 0.01 m considering computational resources. Therefore, the near-wall  $y^+$  value was approximately 30~100, which applied to the wall function. The overall grid quality of the computational grid was kept at 0.3 to 1.0, with the partial quality below 0.3 (approximately 0.01%) due to dense grids. The total number of grids reached 8 million.

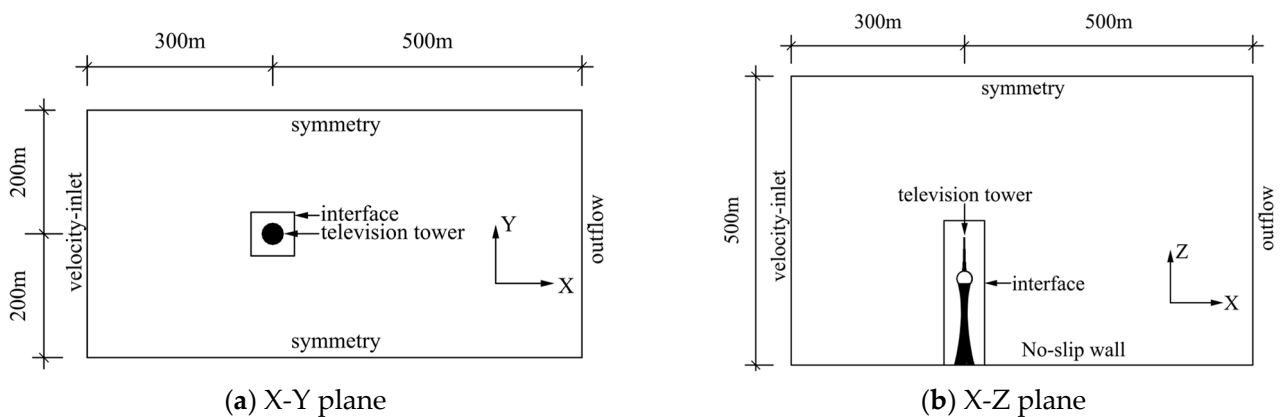


Figure 18. Boundary conditions of the computational domain and definition of the coordinate system.

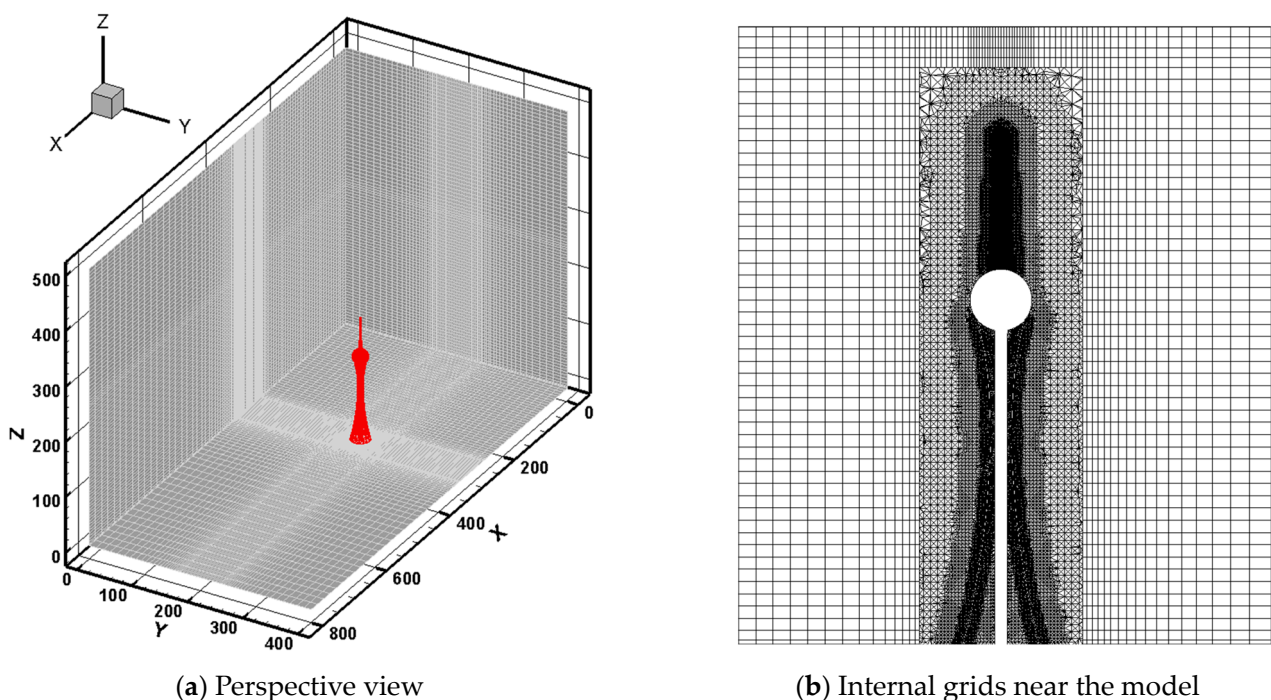


Figure 19. Meshing of the computational domain.

The wall-adapting local eddy-viscosity model was adopted as the subgrid-scale model for LES. The discrete system of the continuity equation is solved using the SIMPLEC algorithm according to the semi-implicit method for solving the pressure-coupled systems of equations. The time derivative was discretized by the second-order implicit scheme, and

the momentum discretization was discretized by the bounded central difference scheme. An absolute velocity residual of less than  $10^{-5}$  was adopted to ensure the convergence of the simulation. The time step for the unsteady LES calculation was set at 0.05 s considering the mesh discretization and computational resources. A total of 600 time steps were resolved to provide a statistically steady result of 30 s. The simulated results from the LES are sampled after an initialization period of 10 s. The specific turbulence characteristic parameters at the inlet are shown in Table 3, where the mean wind speed profile  $U$  and the turbulence intensity  $I_u$  refer to the Chinese code [4]. The recommended values of ESDU 85,020 [36] were adopted for the along-wind turbulence integral scale  $L$ , the turbulence intensity, and the integral scales of the fluctuating components  $v$  and  $w$ .  $z_0 = 0.05$  m,  $c_1 = 10$ ,  $c_2 = 12$ ,  $c_3 = 12$ ,  $\gamma_1 = 2.25$ ,  $\gamma_2 = 2.10$ ,  $\gamma_3 = 2.10$  [39]. The wind load is calculated based on the basic wind pressure of a 50-year recurrence period, and the ground roughness type corresponds to category B in the Chinese code [4].

## 4. Results and Discussions

### 4.1. Distribution of the Velocity Field

Figures 20 and 21 present the instantaneous wind speed contours and streamlines of the three models at 20 s in two planes of  $Y = 200$  m and  $Z = 50$  m at a  $0^\circ$  wind direction angle, respectively. When the incoming wind flows around two sides of the TV tower with the grid structure, part of the incoming wind flows through the grid structure and then acts on the core tube. It separates on the two sides of the core tube and converges on the leeward side, producing dense vortices. Then, the dense vortices are discharged downstream through the grid structure in the leeward zone under the transport of the incoming wind. Yan, B.W. [27] conducted LES simulations on an aero control tower with an elliptical shape. When the incoming flow wind acts on the aero control tower, a relatively long wake zone and quite strong turbulent vortex shedding are found in the numerical simulations, which is quite different from the TV tower with the grid structure.

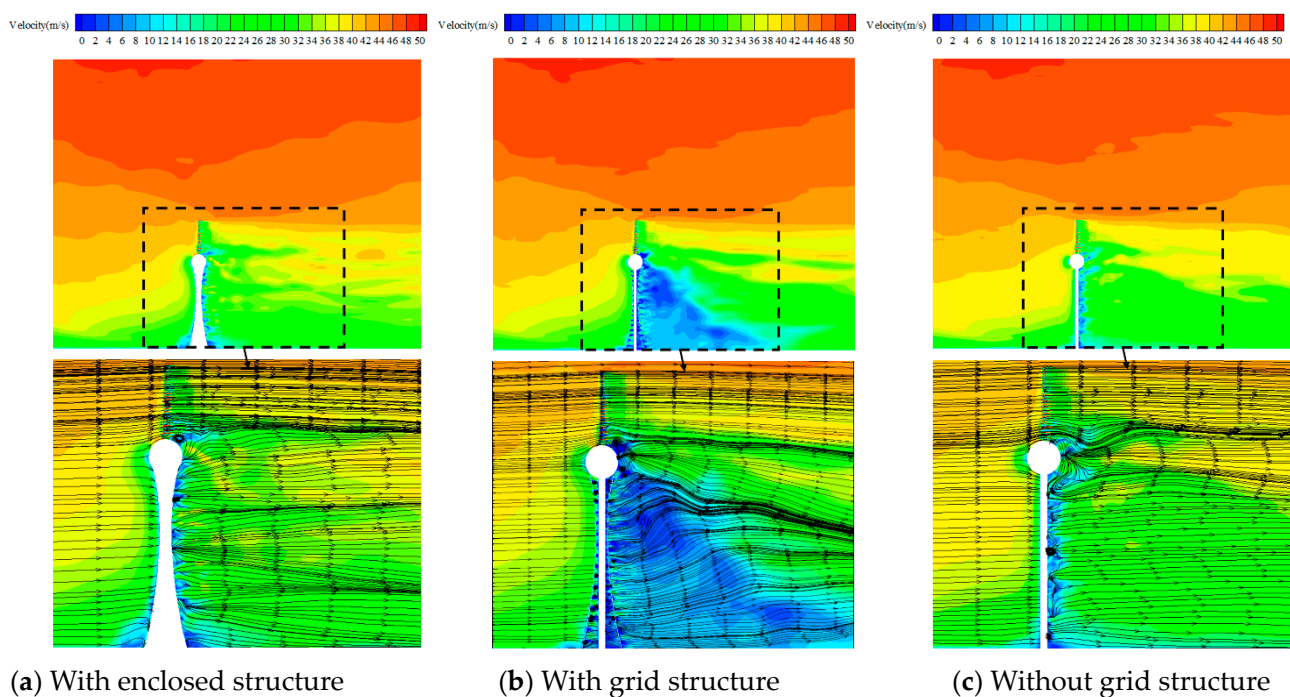


**Figure 20.** Instantaneous wind speed contours and streamlines of the three models at 20 s in the plane of  $Y = 200$  m.

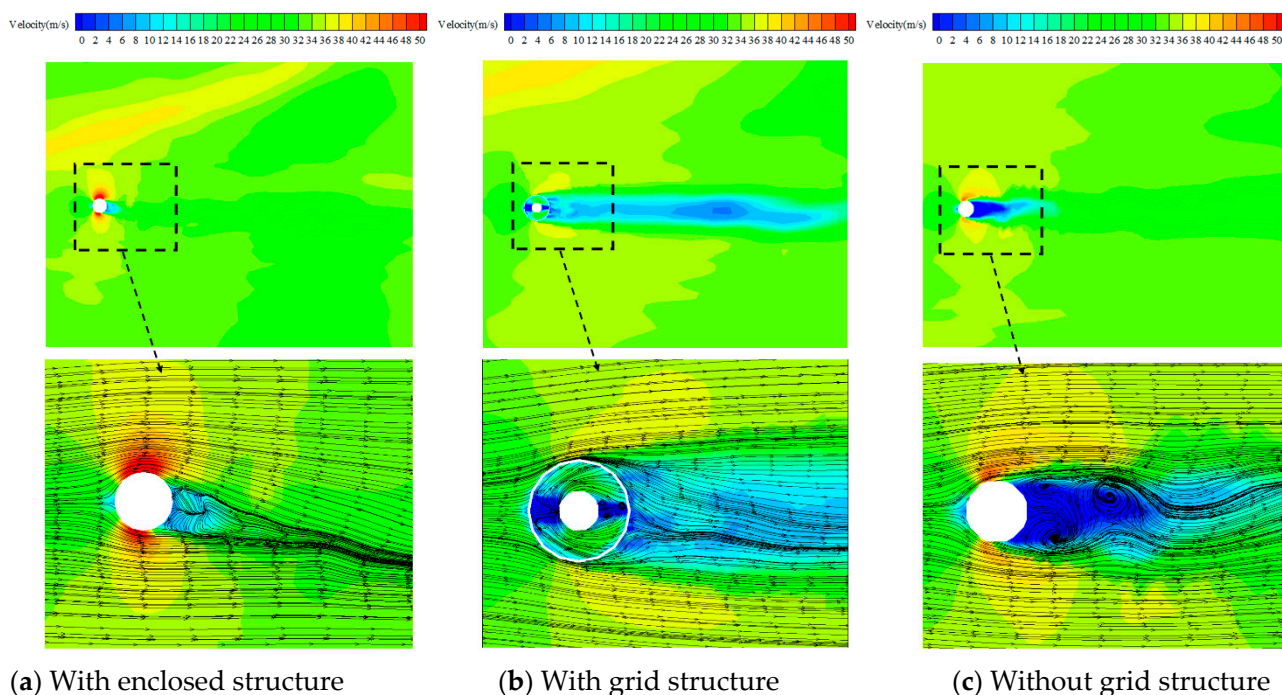


**Figure 21.** Instantaneous wind speed contours and streamlines of the three models at 20 s in the plane of  $Z = 50$  m.

The wake of the model with the grid structure is the longest among the three models. Due to the absence of shading in front of the incoming flow, dense alternating vortices are produced in the leeward zone of the core tube under the interaction of wind speed fluctuations of different frequencies and the vortices in the flow separation zone, with the vortex shedding phenomenon on the lateral side. However, there are only a few small-scale vortices on the leeward and flow separation sides of the core tube, and there is no apparent vortex shedding. Most of the incoming winds converge on the leeward zone and flow out downstream along the incoming path, resulting in the smaller cross-wind load of the grid structure.

#### 4.2. Local Wind Pressure Characteristics on the Outer Surface of the TV Tower with the Grid Structure

Figures 22 and 23 present the mean and fluctuating wind pressure coefficient contours on the outer surface of the grid structure and the core tube of the model with the grid structure at the  $0^\circ$  wind direction angle. The distribution of mean and fluctuating wind pressure coefficients on a 50 m layer at a  $0^\circ$  wind direction angle is shown in Figures 24 and 25. The mean wind pressure on the surface of the core tube with the grid structure in front of the incoming flow is relatively lower than the case without the grid structure. The fluctuating wind pressure on the surface of the core tube in the windward zone is small in the middle and large at the ends, which is attributed to the shading effect of the grid structure, decreasing the wind speed and turbulence intensity of the incoming wind. At the edge of the grid structure and core tube, a higher negative pressure appears because of the flow separation, and the edge of the core tube is relatively more apparent. The maximum negative wind pressure coefficient can reach  $-1.0$ . Moreover, in the leeward zone under the control of the wake, the wind pressures are negative, with small absolute values. Fluctuating wind pressures at the intersection of the rods of the grid structure are smaller than those on the adjacent rods because the wind-affected area at the intersection is larger than the rods, resulting in a more significant influence on the fluctuating dissipation of the wake. This causes the vortices formed by the wake flowing through to influence the adjacent rods, enhancing the fluctuating characteristics and wind pressure.

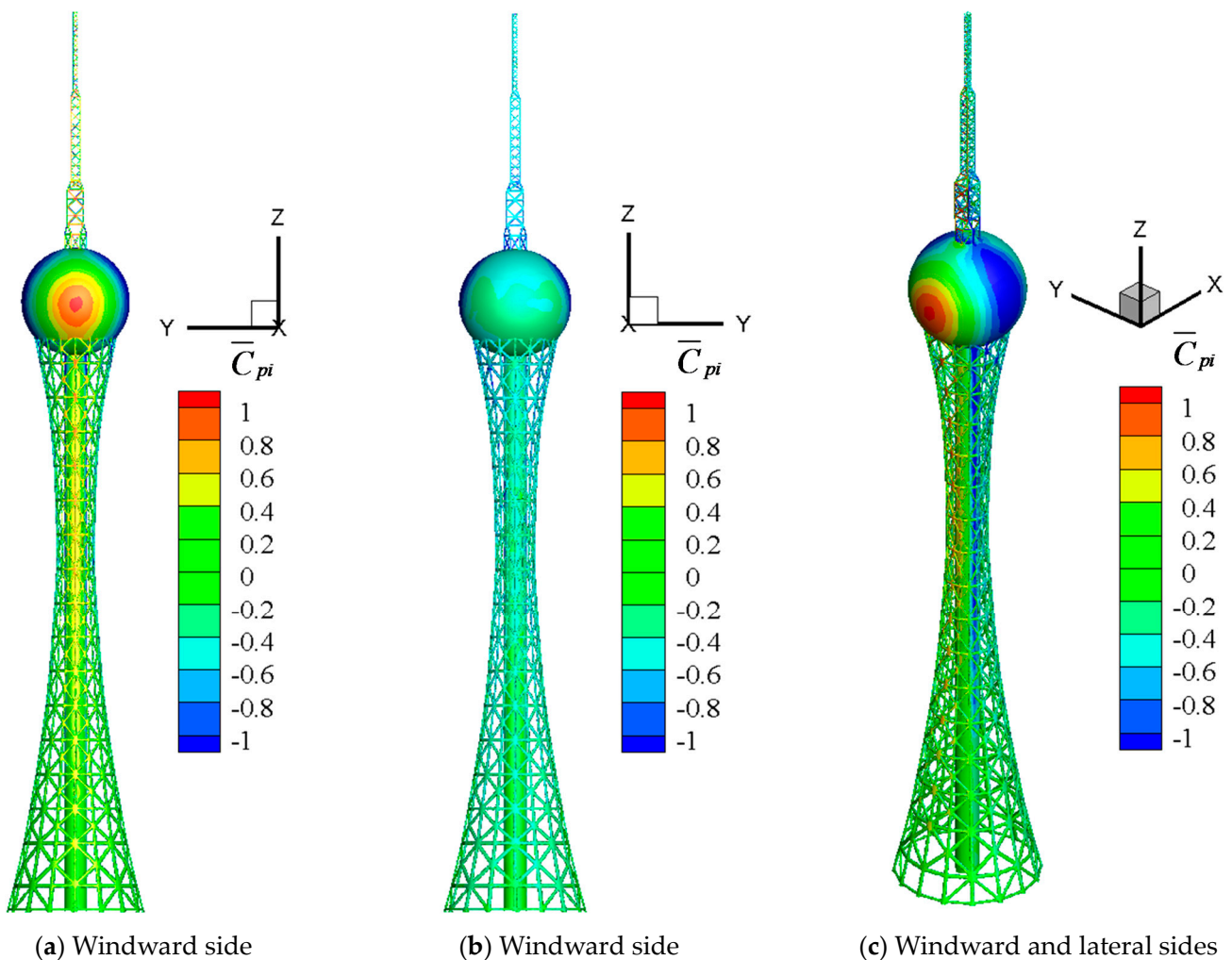


**Figure 22.** Mean wind pressure coefficient distribution of the TV tower with the grid structure.

Figure 26 shows the wind pressure coefficients on the outer surface of the enclosed structure and the grid structure on the 50 m layer at a  $0^\circ$  wind direction angle. The absolute values of mean wind pressures in the windward and leeward zones of the grid structure are slightly higher than that of the enclosed structure, while they are significantly reduced in the flow separation zone compared with the enclosed structure. The fluctuating wind pressure coefficients in the windward zone of the grid structure are close to those of the enclosed structure, while they are significantly smaller in the leeward and flow separation zones, indicating that the intensity of the vortices generated on the lateral side of the grid structure is much less than the case without the grid structure.

Figures 27 and 28 present the mean and fluctuating wind pressure coefficients of each measuring point on the outer surface of the grid structure and the core tube at a  $0^\circ$  wind direction angle. The distribution trends of the mean wind pressure coefficients for each measuring point layer of the grid structure are similar. The absolute values of the mean wind pressure in the windward, flow separation, and leeward zones generally increase as the height increases. The maximum positive pressure appears in the middle of the windward zone (1 measuring point). The mean pressures show a large distribution trend in the middle and a small distribution trend at the ends in the horizontal direction. The maximum mean wind pressure coefficient reaches 0.93. The mean wind pressure coefficients in the flow separation zone are negative and have strong fluctuations. The mean wind pressure coefficients in the leeward zone are relatively stable, fluctuating between  $-0.75$  and  $-0.25$ . The fluctuating wind pressure coefficients are the largest in

the middle of the windward zone and then decrease gradually toward the two ends and increase when approaching the flow separation zone, indicating that the fluctuating wind pressures in the lateral zone are mainly related to the characteristic turbulence.

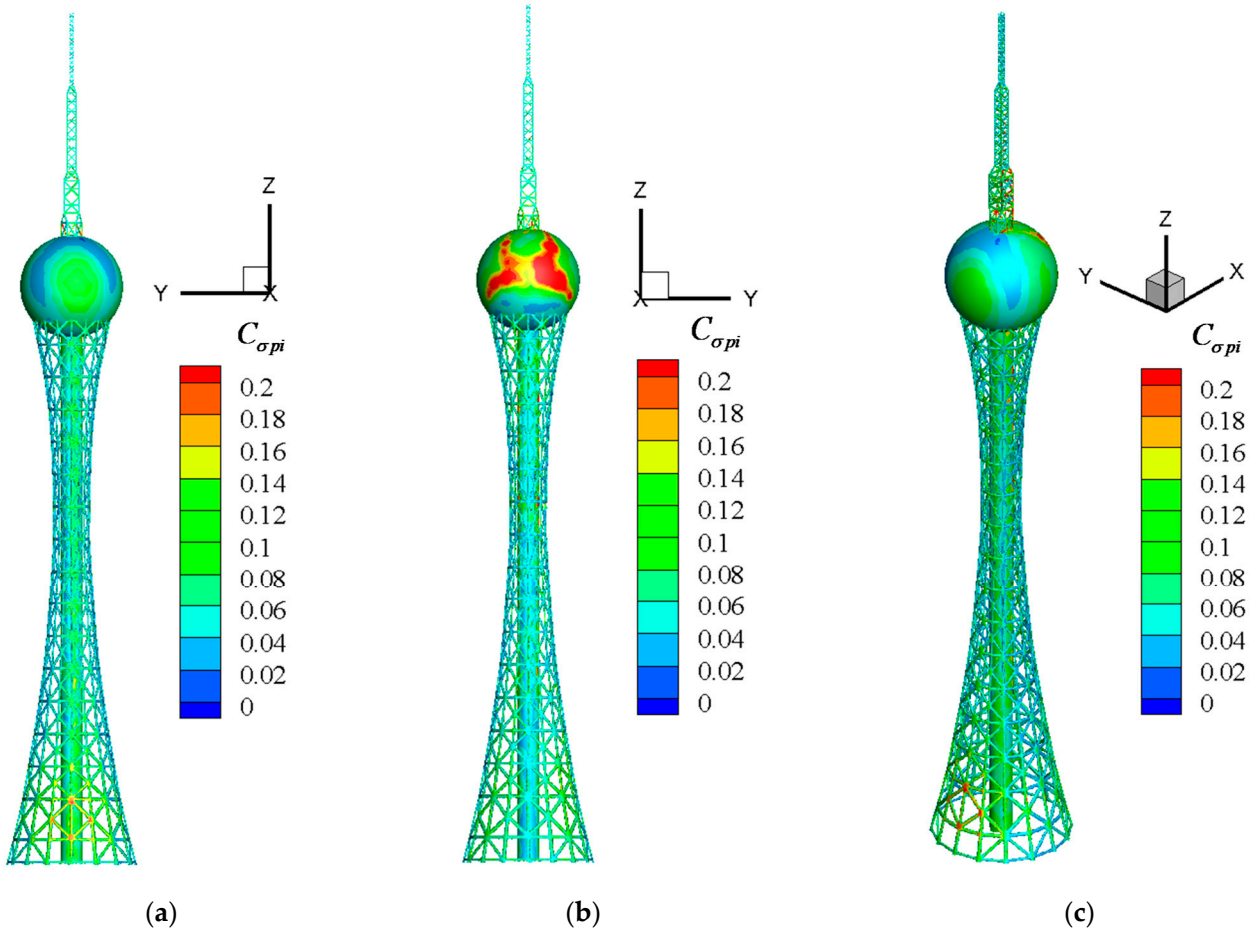


**Figure 23.** Fluctuating wind pressure coefficient distribution of the TV tower with the grid structure. (a) Windward side; (b) Windward side; (c) Windward and lateral sides.

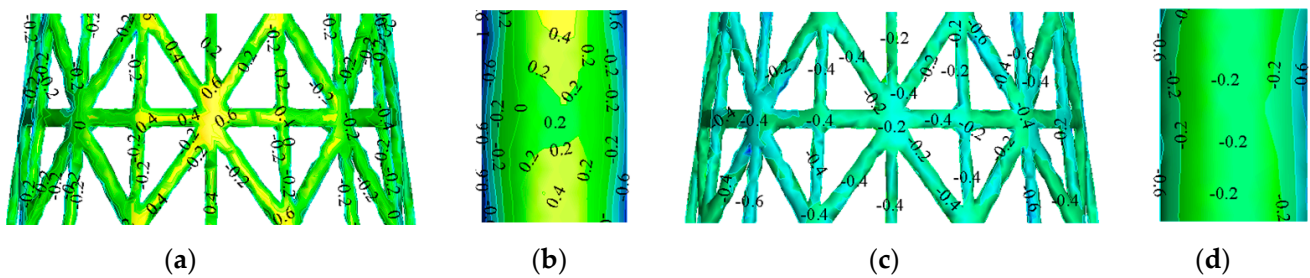


**Figure 24.** Mean wind pressure coefficient distribution on the 50 m layer: (a) Windward side of the grid structure; (b) Windward side of the core tube; (c) Leeward side of the grid structure; (d) Leeward side of the core tube.

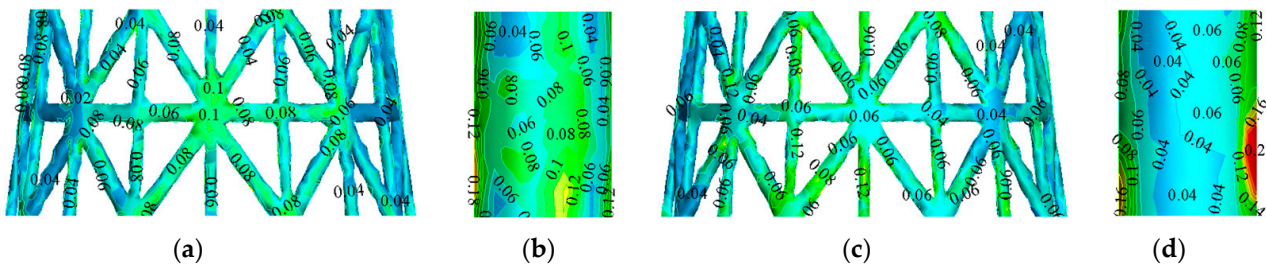


**Figure 25.** Fluctuating wind pressure coefficient distribution on the 50 m layer: (a) Windward side of the grid structure; (b) Windward side of the core tube; (c) Leeward side of the grid structure; (d) Leeward side of the core tube.

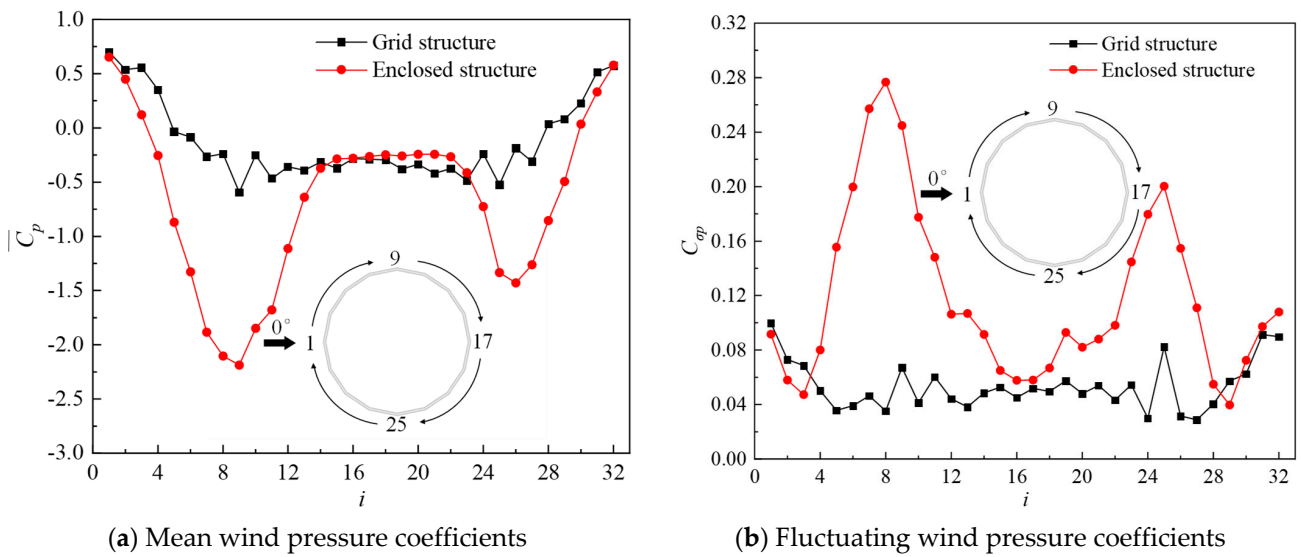


**Figure 26.** Wind pressure coefficients on the outer surface of the enclosed structure and the grid structure on the 50 m layer at a 0° wind direction angle.

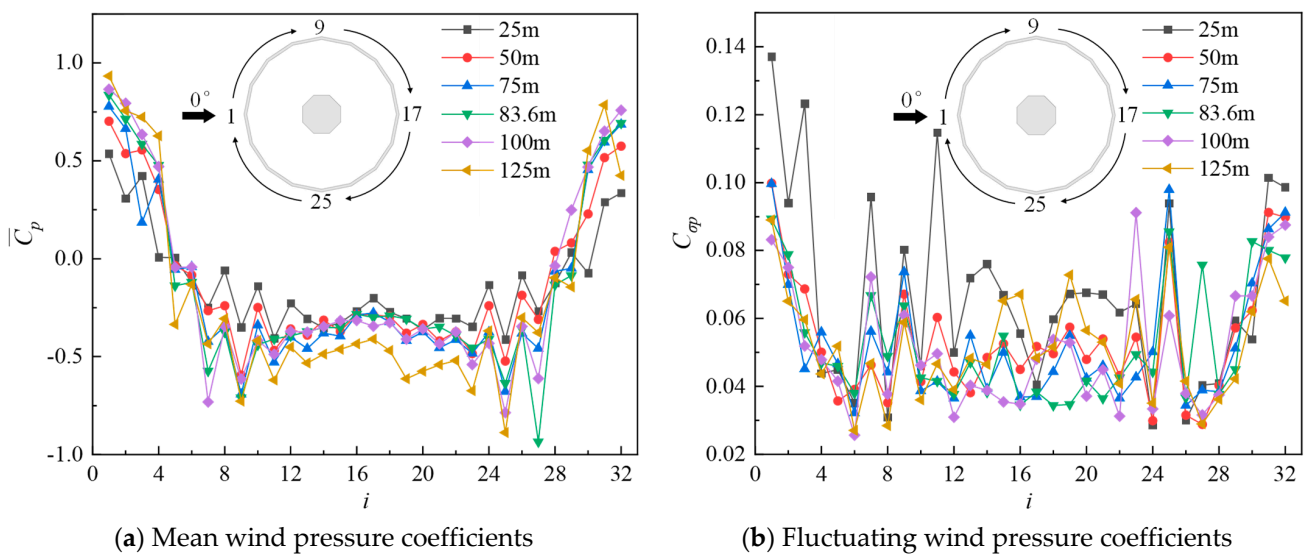


**Figure 27.** Wind pressure coefficients at each measuring point on the outer surface of the grid structure at a 0° wind direction angle.

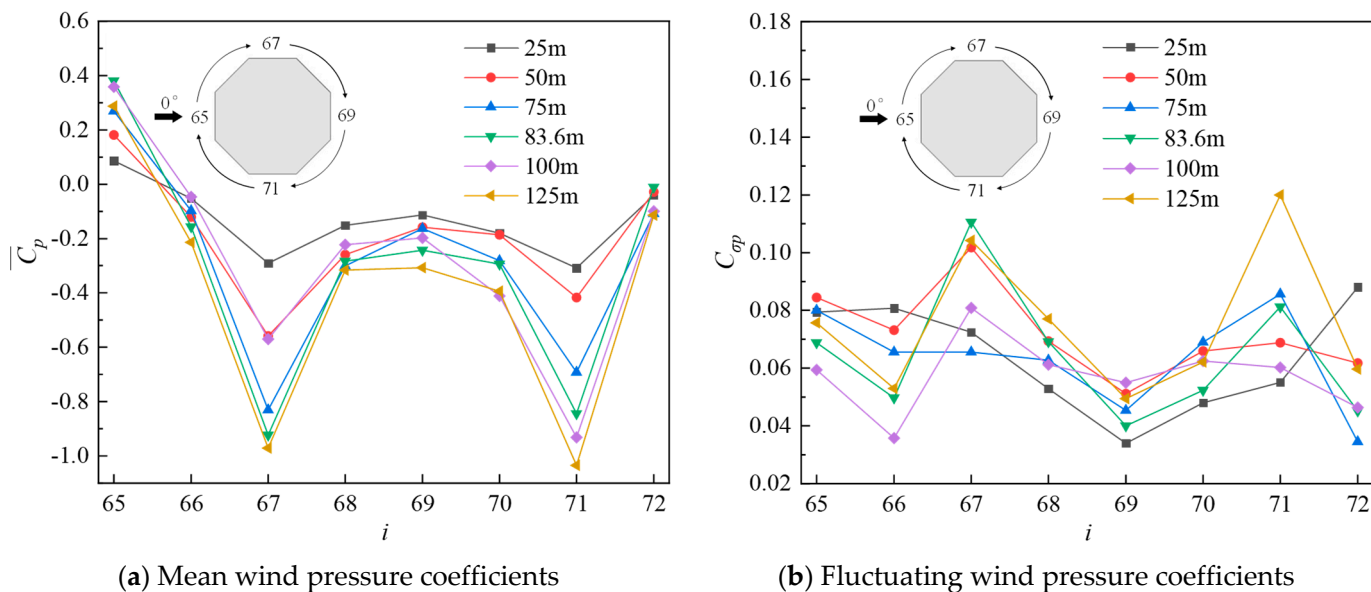


**Figure 28.** Wind pressure coefficients at each measuring point of the core tube at a 0° wind direction angle.

The distribution trend of mean wind pressure coefficients at each measuring point layer of the core tube is similar to that of the outer surface of the grid structure. The maximum positive pressure is in the windward zone (65 measuring point), showing large characteristics in the middle and small characteristics at the ends. The mean wind pressure coefficients are negative in the flow separation and leeward zones (67~71 measuring points). The mean wind pressure coefficients in the leeward zone (68~70 measuring points) vary less, fluctuating between −0.41 and −0.11. The fluctuating wind pressure coefficient reaches the maximum value of 0.12 in the flow separation zone (67, 71 measuring points).

#### 4.3. Power Spectral Densities of Fluctuating Wind Pressure at Typical Measuring Points

The power spectral density can reflect the contribution of wind pressure signals on different frequency bands to the fluctuating wind pressure. Figure 29 shows the normalized power spectra of fluctuating wind pressure at typical measuring points (1, 9, 17, 65, 67, and 69 measuring points) on the 50 m layer at a 0° wind direction angle. The power spectra of the fluctuating wind pressure at each measuring point display a single spectral peak in the 0.04 dimensionless frequency band. The values decrease gradually with the increase in frequency, indicating that the energy of the fluctuating wind pressure is mainly concentrated in the low-frequency region. The power spectra of the flow separation and windward zones are large, while they are small in the leeward zone.

The power spectra of wind pressure on the outer surface of the grid structure (9, 17 measuring points) in the flow separation and leeward zones are lower than those of the enclosed structure, indicating that the shading influence of the grid structure causes the fluctuation characteristics of the incoming flow to reduce. The wind pressure spectra on the outer surface of the grid structure in the windward zone are slightly higher than those of the enclosed structure in the low-frequency band, while they are close in the high-frequency band.

The wind pressure spectral values in the windward zone with the grid structure are higher than those without the grid structure, mainly because the fluctuating characteristics are enhanced by the influence of the vortices generated by the incoming wind flowing through the grid structure. Furthermore, the shading influence of the grid structure causes the vortices to gradually shift from the large-scale vortices generated by the impact to the small-scale vortices, resulting in a decrease in the power spectra of the flow separation and leeward zones compared to the windward zone. Moreover, the wind pressure spectral

values decay rapidly in the high-frequency region, which is mainly related to the turbulent kinetic energy dissipation generated by the numerical algorithm and the filtering of the high-frequency component of the wind velocity-time history by the LES using a filtering function.

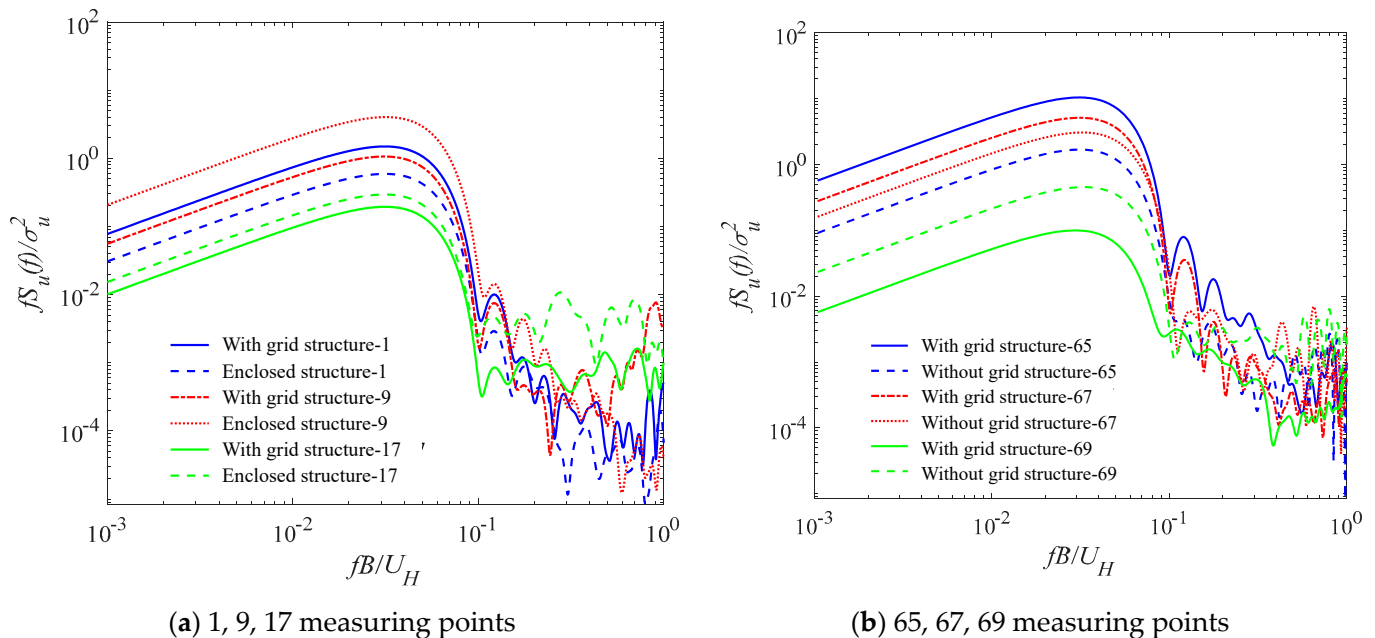


**Figure 29.** Normalized power spectra of fluctuating wind pressure at typical measuring points on the 50 m layer at a  $0^\circ$  wind direction angle.

#### 4.4. Wind Pressure Distribution Characteristics of the Inner and Outer Surfaces of the Grid Structure

The mean, fluctuating, and net wind pressure coefficients on the inner and outer surface of the grid structure on the 50 m layer at a  $0^\circ$  wind direction angle are presented in Figure 30. The inner measuring point numbers 33~64 are transformed into the corresponding outer numbers 1~32 for comparison. The mean wind pressures at the rod intersection on the outer surface of the grid structure in the windward zone are higher than the adjacent rods such as the 1, 2, and 3 measuring points due to the larger wind-affected area and the more obvious obstruction of the incoming wind. Nevertheless, the mean wind pressures at the rod intersection in the leeward and flow separation zones are lower than the adjacent rods such as the 18, 19, and 20 measuring points.

In addition, the corresponding mean and fluctuating wind pressure coefficients on the inner and outer surfaces are different. This discovery is contrary to the results of research on net wind pressures on the inner and outer surface of a torsion-shaped high-rise building with an outer pierced ornament structure [14]. This is mainly because the pierced ornament structure is quite close to the main structure; thus, the inner surface is less affected by wind, indicating that the wind pressures of the grid structure are significantly different from those of other buildings. The distribution trend of the mean wind pressure on the outer surface is the same as the net mean wind pressure. The net wind pressure is greater than that on the outer surface in the windward zone, while it is smaller than that in the leeward zone. This phenomenon is mainly because the surface inside the windward zone is in the leeward zone relative to the outer surface, which shows a negative pressure with a smaller absolute value. Similarly, the surface inside the leeward zone is in the windward zone relative to the outer surface, which shows a smaller positive pressure, increasing or reducing the net wind pressure. Nevertheless, the inner and outer surface pressures in the flow separation zone are negative, such as the 6~11 and 23~27 measuring points. The pressure on the outer surface reaches the minimum value, leading to the absolute value of net wind pressure

being smaller than that on the outer surface. The fluctuating wind pressure distribution characteristics on the inner surface are opposite to those on the outer surface.

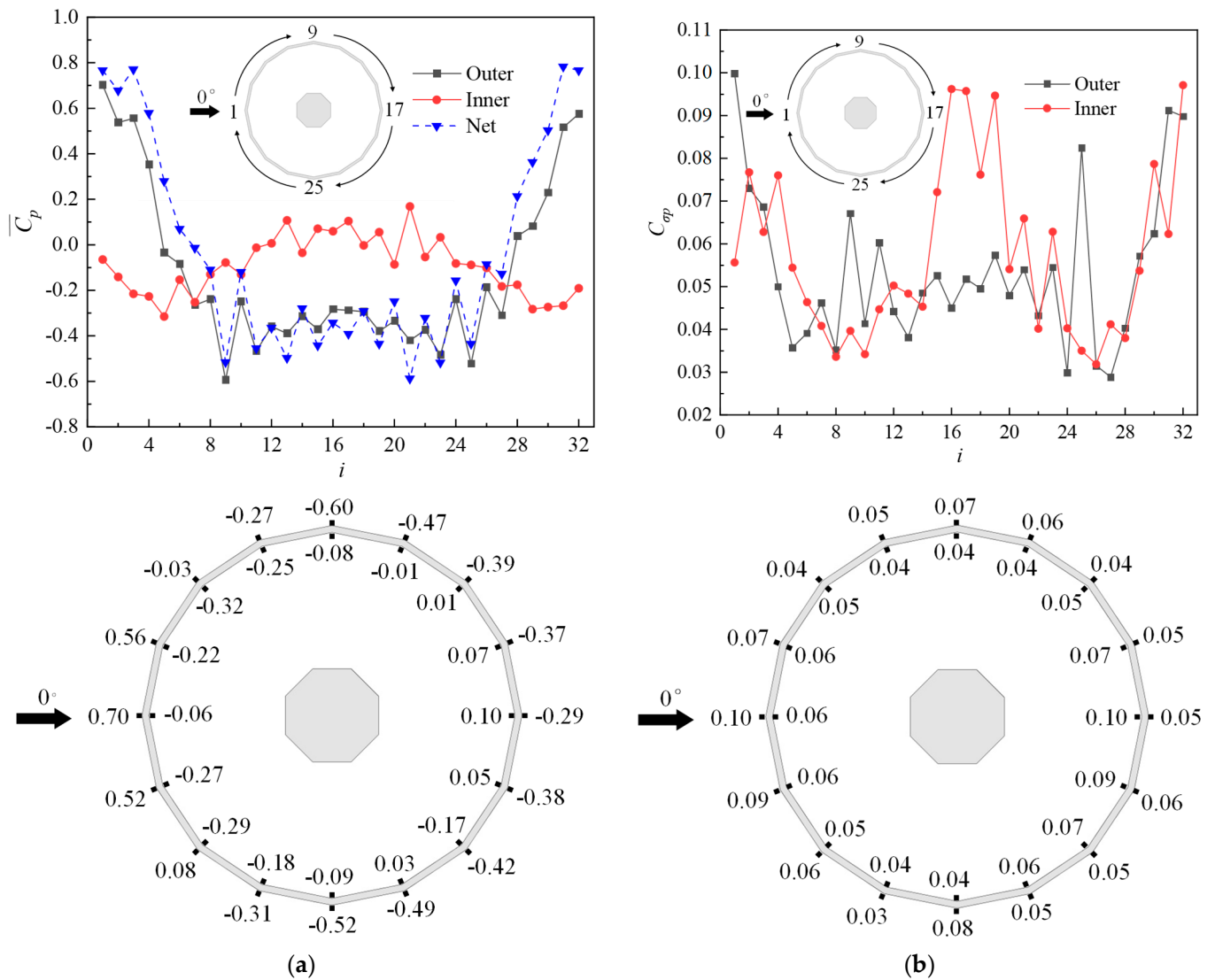


**Figure 30.** Wind pressure coefficients on the inner and outer surface of the grid structure on the 50 m layer at a  $0^\circ$  wind direction angle: (a) Mean wind pressure coefficients at the inner and outer measuring points; (b) Fluctuating wind pressure coefficients at the inner and outer measuring points.

The largest fluctuating wind pressure on the outer surface of the grid structure appears in the middle of the windward zone and gradually reduces toward the flow separation zone at the ends. Then, it increases near the flow separation zone and finally reduces toward the leeward zone. The fluctuating wind pressure on the inner surface in the flow separation zone is relatively small.

#### 4.5. Lift and Drag Coefficients for the TV Tower with a Grid Structure

The drag and lift coefficients— $C_d$  and  $C_l$ , respectively—are calculated according to Equation (6), as follows:

$$C_d = \frac{F_D}{1/2\rho B \int_0^H U(z)^2 dz}, C_l = \frac{F_l}{1/2\rho B \int_0^H U(z)^2 dz} \quad (6)$$

where  $U(z)$  is the mean wind velocity corresponding to the height  $z$ .  $F_D$  and  $F_L$  are the along- and across-wind forces, respectively. Considering the wind shear profile, substituting the velocity profile into the integration one yields:

$$1/2\rho B \int_0^H U(z)^2 dz \approx 0.384\rho BHU_H^2 \tag{7}$$

Figure 31 presents the drag and lift coefficient spectra of the grid structure and the core tube at a  $0^\circ$  wind direction obtained from the numerical simulations. A wide frequency range is presented in the energy spectrum of the drag coefficients. The drag coefficient spectrum of the grid structure is close to that of the total, while it is significantly larger than the core tube, indicating that the along-wind force of the grid structure is relatively large in the total along-wind force. For the lift coefficient spectrum presented in Figure 31b, it appears as a narrow band. The lift coefficient spectra of the grid structure and the core tube reach the maximum at a reduced frequency of approximately 1.44, which is mainly due to the dissipation of the large-scale vortex energy at low frequencies by the grid structure, making the energy transition to high frequencies. However, decay can be observed in the high-frequency region of the drag and lift coefficient spectra of the grid structure and the core tube from simulations. This phenomenon may be caused by the relatively coarse mesh, large time steps, and short iteration times due to the restricted computational resources.

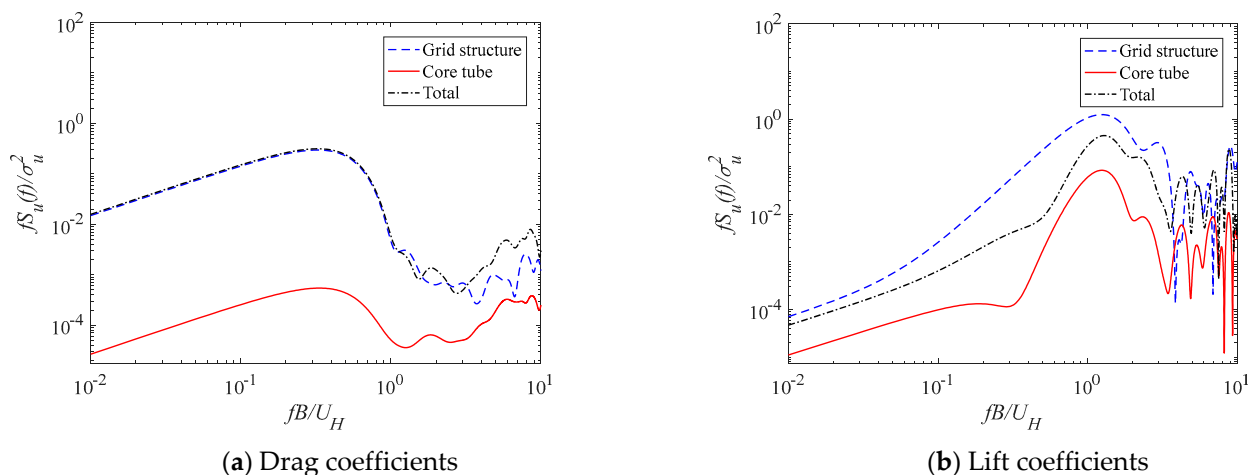


Figure 31. Lift and drag coefficients spectra of the grid structure and the core tube.

#### 4.6. Extreme Net Wind Pressure of the Grid Structure

Figure 32 shows the statistical results of the skewness  $s$  and kurtosis  $k$  of the net wind pressure coefficients of all measuring points at a  $45^\circ$  wind direction angle.  $S$  is concentrated between  $-1$  and  $0.5$ , and  $k$  is concentrated between  $2$  and  $3.5$ , which is similar to the standard normal distribution with skewness  $s = 0$  and kurtosis  $k = 3$ . Similar conclusions can be found for other wind direction angles. Thus, it can be considered that the net wind pressure coefficients of all measuring points approximately obey the Gaussian distribution. Therefore, the extreme net wind pressure coefficients can be obtained by the peak factor method. Figure 33 presents the envelope of the extreme net wind pressure coefficients at measuring points on the outer surface of the grid structure. The maximum and minimum net wind pressure coefficients are calculated according to Equation (8). The extreme net positive pressure at the 13~25 measuring points is lower than others and fluctuates with the wind direction angle, resulting from measuring points not in the vertical windward zone of the incoming wind within the wind direction angle range from  $0^\circ$  to  $90^\circ$ . The extreme negative net pressure varies less with the wind direction angle and fluctuates between  $-1.43$  and  $-0.20$ .

$$C_{npi,max} = \bar{C}_{npi} + 3C_{\sigma pi}, C_{npi,min} = \bar{C}_{npi} - 3C_{\sigma pi} \tag{8}$$

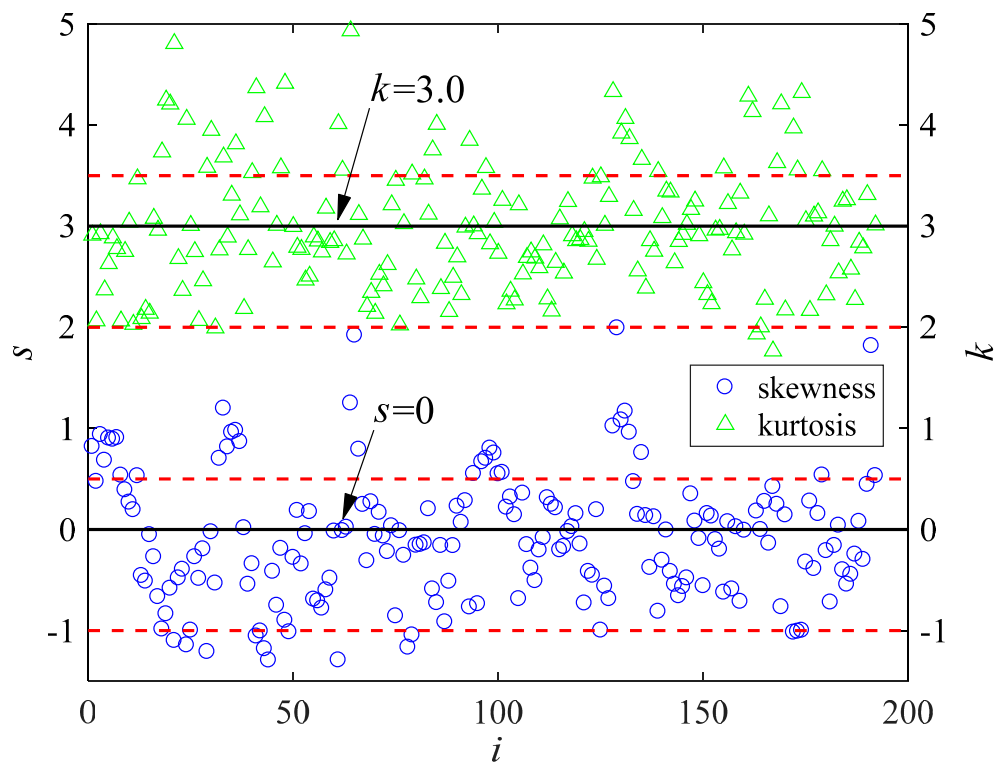


Figure 32. Skewness and kurtosis statistics of the net wind pressure coefficients for all measuring points at a 45° wind direction angle.

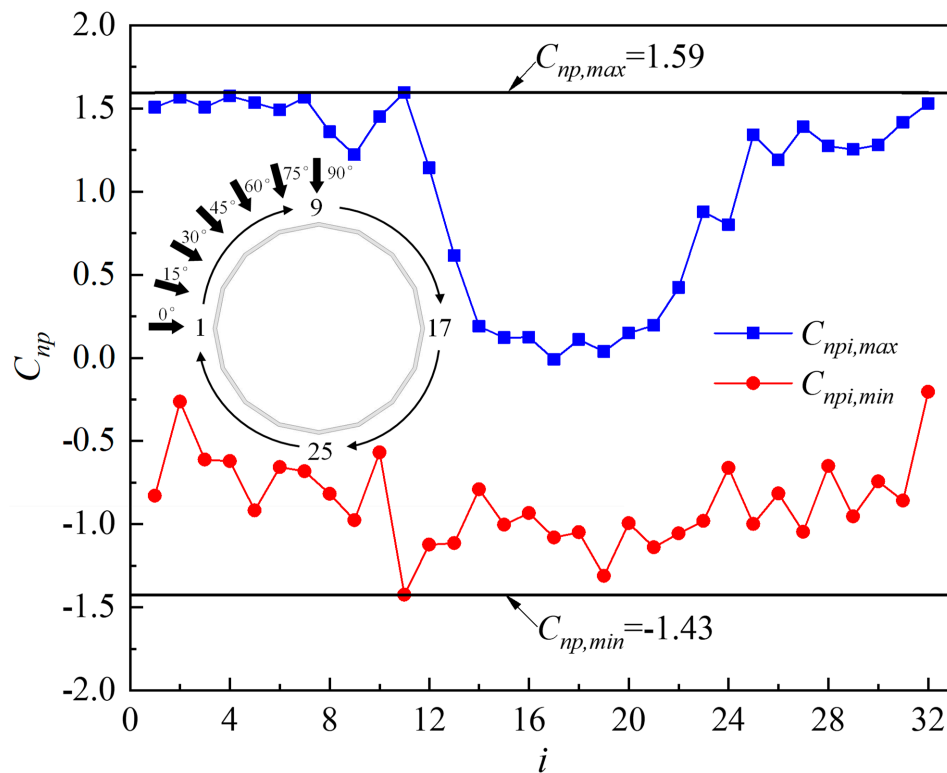


Figure 33. Envelope of the extreme net wind pressure coefficients at measuring points on the outer surface of the grid structure.

#### 4.7. Total Wind Load of the TV Tower with the Grid Structure

The forces ( $F$ ) and moments ( $M$ ) can be calculated by Equations (9a) and (9b), where  $m$  is the number of outermost grids;  $\bar{P}_i$  is the mean static wind pressure over the time history of the grid  $i$ ;  $A_i$  is the surface area of the building corresponding to grid  $i$ ;  $z_i$  is the height corresponding to grid  $i$ ;  $\alpha_i$  is the angle between the  $X$ -axis and the external normal direction of the building surface corresponding to the grid  $i$ .

$$F_X = \sum_{i=1}^m \bar{P}_i A_i \cos \alpha_i, F_Y = \sum_{i=1}^m \bar{P}_i A_i \sin \alpha_i \tag{9a}$$

$$M_X = \sum_{i=1}^m \bar{P}_i A_i z_i \sin \alpha_i, M_Y = \sum_{i=1}^m \bar{P}_i A_i z_i \cos \alpha_i \tag{9b}$$

The resultant wind loads ( $F_X, F_Y$ ) and bending moments ( $M_X, M_Y$ ) of the grid structure and core tube at seven wind direction angles are presented in Figure 34. The along-wind resultant wind load force at the  $0^\circ$  and  $90^\circ$  wind direction angles is significantly larger than the across-wind resultant load force. The maximum positive value of  $F_X$  is obtained at  $15^\circ$  and decreases as the wind direction angle increases in general. In comparison, the maximum negative value of  $F_Y$  is obtained at  $75^\circ$  and increases as the wind direction angle increases in general. The resultant force of the grid structure varies significantly, while that of the core tube varies gently as the wind direction angle changes.

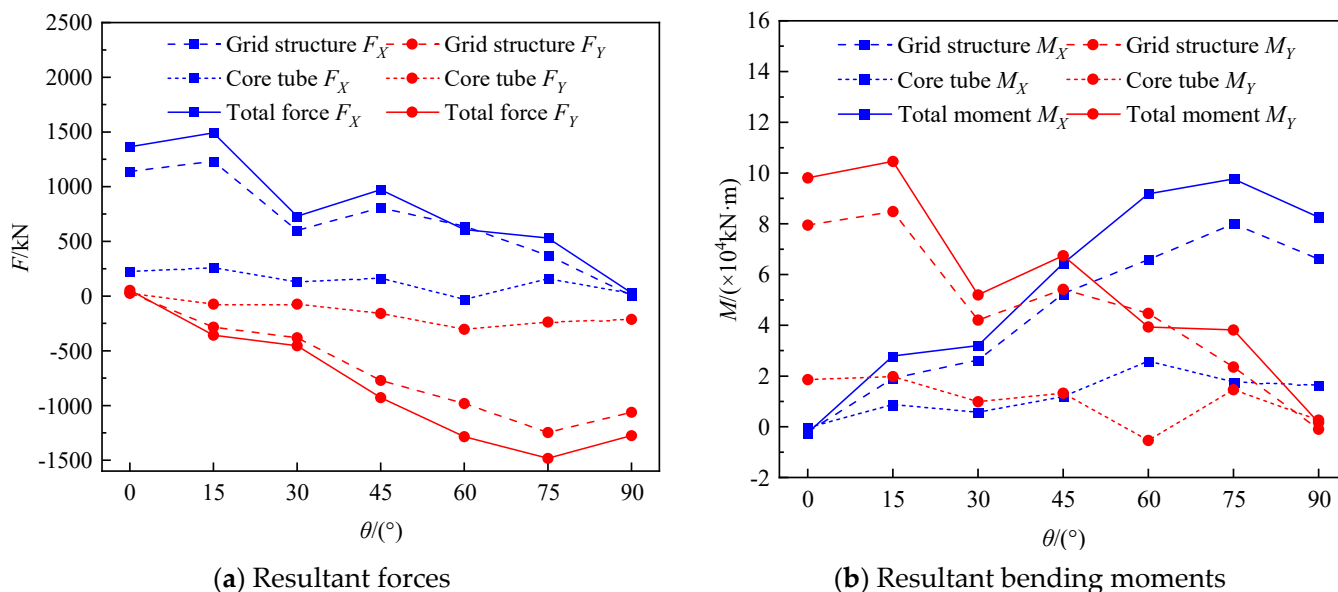


Figure 34. Mean wind load of the grid structure and core tube.

The maximum positive value of  $M_X$  is obtained at  $75^\circ$  and generally increases with the increase in the wind direction angle, while the maximum positive value of  $M_Y$  is obtained at  $0^\circ$  and generally decreases with the increase in the wind direction angle, which is positively related to the absolute value of the resultant force in the  $X$  and  $Y$  directions in general.  $F_X$  and  $F_Y, M_X$  and  $M_Y$  are generally centrally symmetric at a  $45^\circ$  wind direction angle.

Table 4 illustrates the percentage of wind load of the grid structure and core tube in the total wind load. It can be observed that the percentage of wind load of the grid structure in the total wind load is greater than 70%, in general. Furthermore, the percentage of the core tube in several angles exceeds 100% due to the different directions of the grid structure and core tube, such as  $F_X$  and  $M_Y$  at a  $60^\circ$  wind direction angle. At a  $90^\circ$  wind direction angle, although  $F_X$  and  $M_Y$  of the grid structure occupy a relatively smaller proportion of the total wind load, the total load value is small and has no control effect. In conclusion,

the resultant forces and bending moments of the grid structure at all angles exceed 70% of the total wind load and perform a controlling role in the wind load.

**Table 4.** Percentage of wind load of the grid structure and core tube in the total wind load.

Angle (°)	$F_X$		$F_Y$		$M_X$		$M_Y$	
	Grid Structure (%)	Core Tube (%)						
0	83.5	16.5	53.2	46.8	84.8	15.2	81.0	19.0
15	82.6	17.4	79.4	20.6	68.4	31.6	81.1	18.9
30	82.3	17.7	83.8	16.2	82.1	17.9	80.9	19.1
45	83.1	16.9	83.0	17.0	81.5	18.5	80.3	19.7
60	105.0	-5.0	76.4	23.6	71.8	28.2	113.6	-13.6
75	70.1	29.9	84.0	16.0	81.9	18.1	61.7	38.3
90	15.7	84.3	83.3	16.7	80.1	19.9	-58.1	158.1
Mean	74.6	25.4	77.6	22.4	78.7	21.3	62.9	37.1

4.8. Influence of the Grid Structure on the Wind Load of the Core Tube

4.8.1. Wind Pressure Coefficients of the Core Tube with and without the Grid Structure

Figure 35 presents the wind pressure coefficients of the core tube with and without the grid structure on the 75 m layer at a 0° wind direction angle. The shading influence of the grid structure reduces the overall mean wind pressures in the core tube, and the reduction is more evident in the flow separation zone, as measured at the 67 and 71 points. The grid structure can reduce the wind pressure in the flow separation zone of the core tube to a maximum of 50% of that without the grid structure. Moreover, the grid structure can improve the fluctuating wind pressure coefficients in the windward zone of the core tube due to the interference of the grid structure with the incoming wind, which causes the fluctuating characteristics to increase. In the flow separation and leeward zones, the fluctuating wind pressure coefficients decrease, especially in the flow separation zone, due to the shading influence of the grid structure.

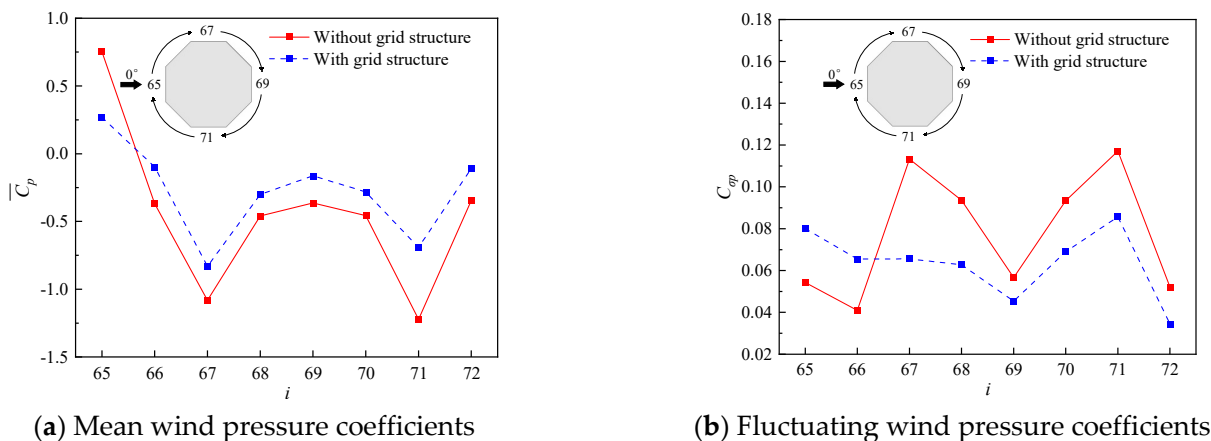


**Figure 35.** Wind pressure coefficients of the core tube with and without the grid structure on the 75 m layer at a 0° wind direction angle.

The mean shape coefficients of the enclosed octagonal building under constant incoming winds are presented in the Chinese code [4] without considering the shading influence of the grid structure. According to the numerical simulation results, Figure 36 and Table 5 present the mean shape coefficients of different wind-affected zones at 0°, 45°, and 90° wind direction angles. The measuring point numbers of different wind-affected zones at different wind direction angles remain the same as they are at the 0° wind direction angle.

The windward and leeward zones of the core tube with the grid structure are substantially reduced compared with the Chinese code. The reduction in the windward zone is greater than that in the leeward zone, with a maximum reduction of 57.5%.

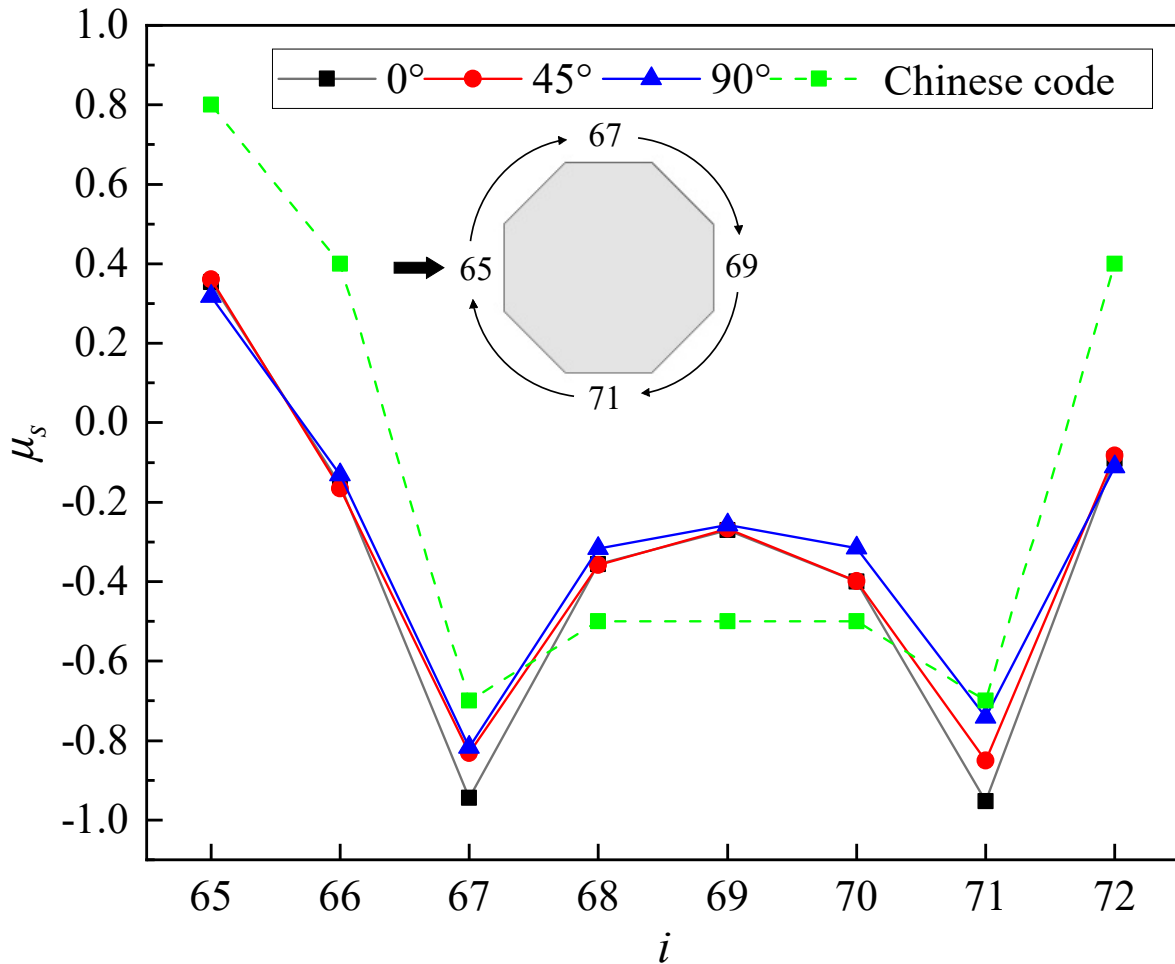
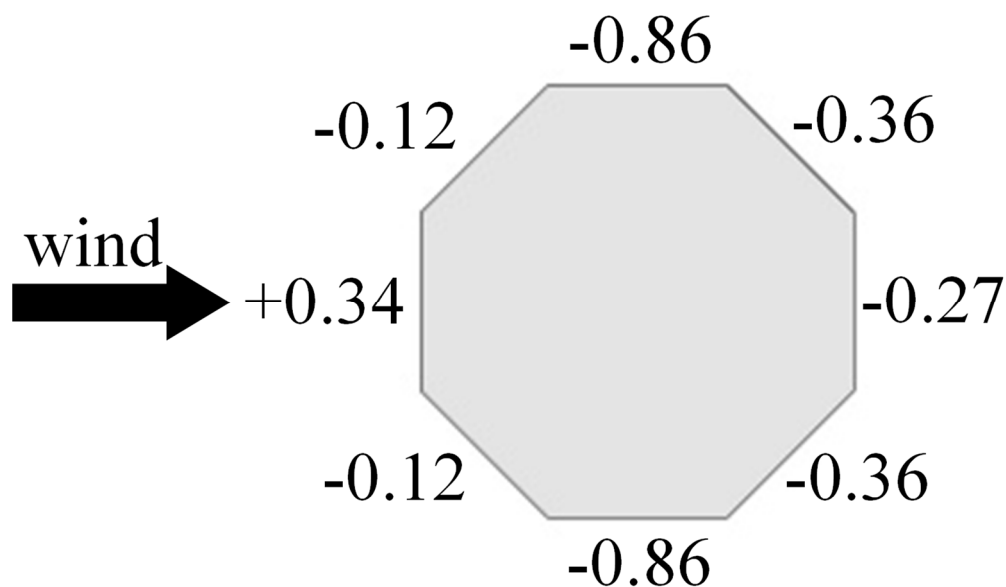


Figure 36. Mean shape coefficients of the different wind-affected zones at 0°, 45°, and 90° wind direction angles.

Table 5. Mean shape coefficients of different wind-affected zones at 0°, 45°, and 90° wind direction angles.

Measuring Point Number	65	66	67	68	69	70	71	72
0°	0.35	-0.16	-0.94	-0.36	-0.27	-0.40	-0.95	-0.09
45°	0.36	-0.17	-0.83	-0.36	-0.26	-0.40	-0.85	-0.08
90°	0.32	-0.13	-0.82	-0.32	-0.26	-0.32	-0.74	-0.11
Mean	0.34	-0.15	-0.86	-0.34	-0.27	-0.37	-0.86	-0.09
Code	0.80	0.40	-0.70	-0.50	-0.50	-0.50	-0.70	0.40
Percentage reduction	57.5%	137.5%	-22.9%	32.0%	46.0%	26.0%	-22.9%	122.5%

Although the grid structure can cause the wind pressure to decrease in the flow separation zone, the absolute value is 23% higher than the reference of the code, which is attributed to the influence of fluctuating characteristics not considered in the code. According to the simulation data, and taking the symmetry into account, the reference values for the mean shape coefficients of the enclosed octagonal cross-section building with the grid structure are presented in Figure 37. The absolute values of simulation in the windward and leeward zones are, on average, 65.8% and 34.7% lower than the code values, respectively, which is beneficial for structural design.



**Figure 37.** Reference values for the mean shape coefficients of the enclosed octagonal cross-section building with the grid structure.

#### 4.8.2. Wind Load of the Core Tube with and without the Grid Structure

The mean resultant wind load forces and bending moments in the X and Y directions of the core tube with and without the grid structure are presented in Figure 38. It can be observed that, except for  $0^\circ$  and  $90^\circ$ , the resultant forces of the core tube with the grid structure in the X and Y directions are smaller than those without the grid structure, with a percentage reduction of 36.3% and 24.3%, respectively. Although the  $F_Y$  of the core tube with the grid structure at a  $0^\circ$  wind direction angle and the  $F_X$  of the core tube with the grid structure at a  $90^\circ$  wind direction angle are smaller than the case without the grid structure, the resultant force value is only 15 kN~30 kN in the X and Y directions. The resultant bending moments of the core tube in the X and Y directions cannot necessarily be reduced due to the grid structure at different wind direction angles, indicating that the grid structure reduces the absolute values of the mean wind pressures of the core tube shaded by the grid structure. However, part of the incoming wind flowing through the grid structure acts directly on the core tube, resulting in a larger wind pressure in the non-shaded part. The overall wind load resultant force and the bending moment of the core tube might increase.

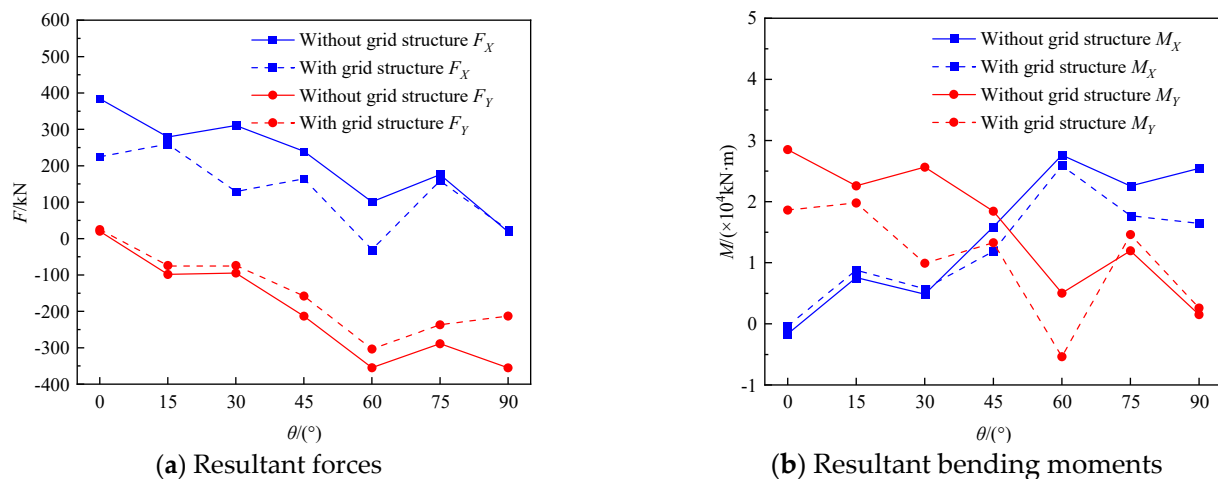


Figure 38. Wind load of the core tube with and without the grid structure.

## 5. Conclusions

This study investigates the wind pressure distribution on the inner and outer surfaces of the grid structure and the influence of the grid structure on the wind pressure and the load of the core tube. According to the simulation results, the shape coefficients of the octagonal building with the grid structure are provided for reference. The main conclusions drawn from this study are as follows:

1. The mean wind pressure at the intersection of rods on the outer surface of the grid structure in the windward zone is higher than that on adjacent rods, while it is lower than that on adjacent rods in the leeward and flow separation zones.
2. The grid structure decreases the mean wind pressures on the outer surface in the flow separation zones and the fluctuating wind pressures in the flow separation and leeward zones. However, the grid structure has little effect on the mean wind pressure in the windward and leeward zones and the fluctuating wind pressures in the windward zone.
3. The absolute value of the net wind pressure is larger than the wind pressure on the outer surface in the windward positive pressure and leeward zones, while it is smaller than that in the flow separation zone. The net wind pressure coefficients of all measuring points approximately obey the Gaussian distribution. The extreme positive net wind pressure coefficient on the outer surface of the grid structure is 1.59, and the extreme negative value is  $-1.43$ .
4. The resultant wind load forces and bending moments in the X and Y directions of the grid structure are relatively larger in the total wind load; they are generally greater than 70%, performing a controlling role in the wind load.
5. The grid structure can reduce the absolute values of the mean wind pressures on the surface of the core tube shaded by the grid structure in the windward zone and the fluctuating wind pressures in the flow separation and leeward zones. The simulated absolute values of the mean shape coefficients of the octagonal cross-section buildings with the grid structure in the windward and leeward zones are, on average, 65.8% and 34.7% lower than the reference of the Chinese code, respectively, while they are 23% higher than the reference of the code in the separation zones.
6. The resultant forces of the core tube with the grid structure in the X and Y directions are smaller than those without the grid structure, with a percentage reduction of 36.3% and 24.3%, respectively.

**Author Contributions:** Conceptualization, R.F.; methodology, P.W. and F.H.; software, P.W. and G.C.; formal analysis, P.W. and G.C.; data curation, P.W., G.C. and F.H.; writing—original draft preparation, P.W.; writing—review and editing, R.F.; visualization, P.W.; supervision, R.F.; project administration, R.F. All authors have read and agreed to the published version of the manuscript.

**Funding:** This research is financially supported by the National Natural Science Foundation of China (Grant number: 51978151).

**Institutional Review Board Statement:** Not applicable.

**Informed Consent Statement:** Not applicable.

**Data Availability Statement:** The data supporting the findings of this research are available on request from the corresponding author. The data are not publicly available due to privacy or ethical restrictions.

**Conflicts of Interest:** The authors declare that they have no known competing financial interest or personal relationships that could have appeared to influence the work reported in this paper.

## References

1. Bandi, E.K.; Tamura, Y.; Yoshida, A.; Kim, Y.C.; Yang, Q.S. Experimental investigation on aerodynamic characteristics of various triangular-section high-rise buildings. *J. Wind Eng. Ind. Aerodyn.* **2013**, *122*, 60–68. [\[CrossRef\]](#)
2. Li, Y.; Li, Q.S.; Chen, F.B. Wind tunnel study of wind-induced torques on L-shaped tall buildings. *J. Wind Eng. Ind. Aerodyn.* **2017**, *167*, 41–50. [\[CrossRef\]](#)
3. Tanaka, H.; Tamura, Y.; Ohtake, K.; Nakai, M.; Kim, Y.C. Experimental investigation of aerodynamic forces and wind pressures acting on tall buildings with various unconventional configurations. *J. Wind Eng. Ind. Aerodyn.* **2012**, *107*, 179–191. [\[CrossRef\]](#)
4. GB50009-2012; Load Code for the Design of Building Structures. China Architecture and Building Press: Beijing, China, 2012.
5. To, A.P.; Lam, K.M.; Wong, S.Y.; Xie, Z.N. Effect of a through-building gap on wind-induced loading and dynamic responses of a tall building. *Wind Struct.* **2012**, *15*, 531–553. [\[CrossRef\]](#)
6. Kikitsu, H.; Okada, H. Open passage design of tall buildings for reducing aerodynamic response. In *Wind Engineering into the 21st Century*; CRC Press: Boca Raton, FL, USA, 1999; pp. 667–672.
7. Li, Y.G.; Zhang, M.Y.; Li, Y.; Li, Q.S.; Liu, S.J. Experimental study on wind load characteristics of high-rise buildings with opening. *Struct. Des. Tall Spec. Build.* **2020**, *29*, e1734. [\[CrossRef\]](#)
8. Holmes, J.D. Along-wind responses of lattice tower, part I-derivation of expressions for gust response factors. *Eng. Struct.* **1994**, *16*, 287–292. [\[CrossRef\]](#)
9. Liang, S.G.; Zou, L.H.; Zhao, L.; Ge, Y.J. Experimental study of three-dimensional dynamic wind loads on lattice towers in wind tunnel. *J. Aerodyn.* **2007**, *3*, 311–318.
10. Yang, F.; Dang, H.; Niu, H.; Zhang, H.; Zhu, B. Wind tunnel tests on wind loads acting on an angled steel triangular transmission tower. *J. Wind Eng. Ind. Aerodyn.* **2016**, *156*, 93–103. [\[CrossRef\]](#)
11. Zhou, Q.; Zhao, L.T.; Zhu, Q.; Zhu, Y.F. Mean wind loads on equilateral triangular lattice tower under skewed wind loading. *J. Wind Eng. Ind. Aerodyn.* **2021**, *208*, 104467. [\[CrossRef\]](#)
12. Li, Z.L.; Liu, X.P.; Yan, Z.T.; Xiao, Z.Z.; Yu, D.K. Experimental study on wind characteristics of sheltered lattice towers. *Vib. Shock* **2015**, *34*, 99–104.
13. Hu, G.; Hassanli, S.; Kwok, K.C.S.; Tse, K.T. Wind-induced responses of a tall building with a double-skin facade system. *J. Wind Eng. Ind. Aerodyn.* **2017**, *168*, 91–100. [\[CrossRef\]](#)
14. Shen, G.H.; Qian, T.; Yang, X.Q.; Fang, H.Q.; Lou, W.J. Study on wind load of torsional body type high-rise building with external openwork decorative structure. *J. Build. Struct.* **2013**, *34*, 68–74.
15. Yang, X.Y.; Qin, W.F.; Ke, Y.Y.; Xie, J.M. Influence of skeletonized double-layer curtain wall on structural wind response of high-rise buildings. *J. Harbin Inst. Technol.* **2021**, *53*, 70–78.
16. Guichard, R. Assessment of an improved Random Flow Generation method to predict unsteady wind pressures on an isolated building using Large-Eddy Simulation. *J. Wind Eng. Ind. Aerodyn.* **2019**, *189*, 304–313. [\[CrossRef\]](#)
17. Pamiès, M.; Weiss, P.; Garnier, E.; Deck, S.; Sagaut, P. Generation of synthetic turbulent inflow data for large eddy simulation of spatially evolving wall-bounded flows. *Phys. Fluids* **2009**, *21*, 045103. [\[CrossRef\]](#)
18. Dhamankar, N.S.; Blaisdell, G.A.; Lyrintzis, A.S. Overview of Turbulent Inflow Boundary Conditions for Large-Eddy Simulations. *AIAA J.* **2018**, *56*, 1317–1334. [\[CrossRef\]](#)
19. Kraichnan, R.H. Diffusion by a random velocity field. *Phys. Fluids* **1970**, *13*, 22–31. [\[CrossRef\]](#)
20. Smirnov, A.; Shi, S.; Celik, I. Random flow generation technique for large eddy simulations and particle-dynamics modeling. *J. Fluids Eng.* **2001**, *123*, 359–371. [\[CrossRef\]](#)
21. Huang, S.H.; Li, Q.S.; Wu, J.R. A general inflow turbulence generator for large eddy simulation. *J. Wind Eng. Ind. Aerodyn.* **2010**, *98*, 600–617. [\[CrossRef\]](#)

22. Castro, H.G.; Paz, R.R. A time and space correlated turbulence synthesis method for Large Eddy Simulations. *J. Comput. Phys.* **2013**, *235*, 742–763. [[CrossRef](#)]
23. Aboshosha, H.; Elshaer, A.; Bitsuamlak, G.T.; El Damatty, A. Consistent inflow turbulence generator for LES evaluation of wind-induced responses for tall buildings. *J. Wind Eng. Ind. Aerodyn.* **2015**, *142*, 198–216. [[CrossRef](#)]
24. Yu, Y.L.; Yang, Y.; Xie, Z.N. A new inflow turbulence generator for large eddy simulation evaluation of wind effects on a standard high-rise building. *Build. Environ.* **2018**, *138*, 300–313. [[CrossRef](#)]
25. Ji, B.F.; Lei, W.Z.; Xiong, Q. An inflow turbulence generation method for large eddy simulation and its application on a standard high-rise building. *J. Wind Eng. Ind. Aerodyn.* **2022**, *226*, 105048. [[CrossRef](#)]
26. Vranešević, K.K.; Vita, G.; Bordas, S.P.A.; Gluma, A.S. Furthering knowledge on the flow pattern around high-rise buildings: LES investigation of the wind energy potential. *J. Wind Eng. Ind. Aerodyn.* **2022**, *226*, 105029. [[CrossRef](#)]
27. Yan, B.W.; Li, Q.S. Detached-eddy and large eddy simulations of wind effects on a high-rise structure. *Comput. Fluids* **2017**, *150*, 74–83. [[CrossRef](#)]
28. Wang, H.; Hou, X.; Deng, Y. Numerical simulations of wind-driven rain on building facades under various oblique winds based on Eulerian multiphase model. *J. Wind Eng. Ind. Aerodyn.* **2015**, *142*, 82–92. [[CrossRef](#)]
29. Lu, C.; Li, Z.; Li, Q. Wind-induced response analysis of Taipei 101 building based on large eddy simulation. *J. Vib. Shock* **2019**, *38*, 172–181.
30. Huang, S.; Li, R.; Li, Q.S. Numerical simulation on fluid-structure interaction of wind around super-tall building at high Reynolds number conditions. *Struct. Eng. Mech.* **2013**, *46*, 197–212. [[CrossRef](#)]
31. Yu, Y.L.; Yang, Y.; Liu, F.J.; Shi, B.Q.; Xie, Z.N. Large eddy simulation for wind induced responses of Nanning Wuxiang ASEAN Tower. *J. Vib. Shock* **2018**, *37*, 78–86.
32. Dagnew, A.K.; Bitsuamlak, G.T. Computational evaluation of wind loads on a standard tall building using LES. *Wind Struct.* **2014**, *18*, 567–598. [[CrossRef](#)]
33. Blocken, B. 50 years of Computational Wind Engineering, Past, present and future. *J. Wind Eng. Ind. Aerodyn.* **2014**, *129*, 69–102. [[CrossRef](#)]
34. Murakami, S. Overview of turbulence models applied in CWE–1997. *J. Wind Eng. Ind. Aerodyn.* **1998**, *74*, 1–24. [[CrossRef](#)]
35. Tominaga, Y.; Mochida, A.; Yoshie, R.; Kataoka, H.; Nozu, T.; Yoshikawa, M.; Shirasawa, T. AIJ guidelines for practical applications of CFD to pedestrian wind environment around buildings. *J. Wind Eng. Ind. Aerodyn.* **2008**, *96*, 1749–1761. [[CrossRef](#)]
36. Engineering Sciences Data Unit (ESDU). *Characteristics of Atmospheric Turbulence Near the Ground. Part II, Single Point Data for Strong Winds*; Report No. ESDU 85020; Engineering Sciences Data Unit: London, UK, 2001.
37. *ASCE/SEI 7-05*; Minimum Design Loads for Buildings and Other Structures. ASCE: Reston, VA, USA, 2006.
38. *AS/NZS 1170.3:2003*; Australian/New Zealand Standard. Structural design actions. Standards Australia: Sydney, NSW, Australia, 2003.
39. Hu, X.B.; Yang, Y. Study on the simulation of large eddies in wind fields in standard landscapes based on NSRFG method. *Eng. Mech.* **2020**, *37*, 112–122.